Influence of the fiber geometry on the macroscopic elastic and thermal properties

Hellen Altendorf, Dominique Jeulin, François Willot

▶ **To cite this version:**

Hellen Altendorf, Dominique Jeulin, François Willot. Influence of the fiber geometry on the macroscopic elastic and thermal properties. International Journal of Solids and Structures, 2014, 51 (23-24), pp.3807-3822. 10.1016/j.ijsolstr.2014.05.013 . hal-01002835v1

HAL Id: hal-01002835

https://hal.science/hal-01002835v1

Submitted on 6 Jun 2014 (v1), last revised 30 May 2019 (v3)

HAL is a multi-disciplinary open access archive for the deposit and dissemination of scientific research documents, whether they are published or not. The documents may come from teaching and research institutions in France or abroad, or from public or private research centers.

L'archive ouverte pluridisciplinaire **HAL**, est destinée au dépôt et à la diffusion de documents scientifiques de niveau recherche, publiés ou non, émanant des établissements d'enseignement et de recherche français ou étrangers, des laboratoires publics ou privés.

Influence of the fiber geometry on the macroscopic elastic and thermal properties

Hellen Altendorf[a,*], Dominique Jeulin[a], François Willot[a]

[a] *Mines ParisTech, Centre de Morphologie Mathématique, Mathématiques et Systèmes, 35 rue Saint Honoré, 77305 Fontainebleau cedex, France.*

Abstract

This work focuses on the linear elastic and thermal properties of real and virtual, computer-generated fibrous composites. A stochastic microstructure model is used to generate densely-assembled 3D systems of curved, non overlapping fibers with specific orientation distributions. This model is first optimized to approach the characteristics of a real fiber glass polymer by fitting geometrical and statistical parameters, such as fiber orientation, radius, length, and curvature. Second, random realizations of the stochastic models that depart from the characteristics of the fiber glass polymer are generated. The latter, which range from isotropic to transversely isotropic and to orthotropic materials, represent plausible virtual fibrous materials. Full-field numerical computations, undertaken by means of the Fourier-based (FFT) method, are used to estimate the local and effective mechanical and thermal

*Corresponding author.

Email addresses: hellen.altendorf@mines-paristech.fr (Hellen Altendorf), dominique.jeulin@mines-paristech.fr (Dominique Jeulin), francois.willot@mines-paristech.fr (François Willot)

[0] Abbreviations: FFT - Fast Fourrier Transform; RVE - Representative Volume Element; GRP - Glass-Fiber Reinforced Polymer; HS - Hashin-Shtrikman; MPa - Mega Pascal

responses of the fibrous composites. The anisotropy of the macroscopic responses as well as the size of the corresponding representative volume element (RVE) are examined numerically. It is found that the variance of the properties on a volume V scales as a powerlaw $\sim 1/V^{\alpha}$ where $\alpha < 1$, an effect of long-range correlations in the microstructure. Finally, the overall behavior of the fiber composites are computed for varying fiber curvature and orientation distributions, and compared with available analytical bounds. We find that the fiber arrangement strongly influences the elastic and thermal responses, less so for the fiber curvature.
Keywords: Glass fiber reinforced polymer, FFT computation, stochastic modeling, linear elasticity, thermal conductivity, representative volume element.

1. Introduction

The use of fibrous composites has recently increased in vast areas of material engineering, such as in aeronautics and automotive industry. Their physical properties largely depend upon the materials microstructure and fibers arrangement which 2D models can not take into account; accordingly, a detailed analysis of these materials is required to estimate and understand their macroscopic behavior. The final goal is to optimize fibrous materials by means of "virtual material design". New fibrous materials are virtually created as realizations of a stochastic model and evaluated with physical simulations. This allows for material optimization for a specific use, without constructing expensive prototypes or performing mechanical experiments.

In order to design a practically fabricable material, a stochastic model is

designed and adapted to an existing material and then slightly modified. The virtual reconstruction of the existing material requires a precise knowledge of the geometry of its microstructure. We propose and apply a local analysis of fiber orientation and radius as well as a single fiber tracking approach to characterize in details the fiber system. In this work, the theory used to simulate and interpret the elastic and thermal properties of fiber-reinforced materials is presented, and then applied to a glass-fiber reinforced polymer.

This paper is structured in three parts. The first part on image analysis and stochastic modeling is used to generate realizations of virtual materials of fiber systems. The second part is devoted to the local and effective constitutive laws of the material, in mechanics and conductivity, as well as the numerical method used to solve them. Finally, the method is applied to a sample of glass fiber reinforced composite.

2. Microstructure characterization and stochastic models for fibrous composites

In this section, the fibrous microstructure, its virtual reconstruction, that serves as a basis for the physical simulations, and the stochastic fiber models are presented. We first introduce the material, glass fiber reinforced polymer, which is the subject of our application. A fiber tracking approach enables the complete quantification of the fiber system with amount, length, radius and curvature. Realizations of two stochastic models are considered: the standard Boolean system of (straight) cylinders and a complex fiber packing approach, more representative of the measured characteristics of the real microstructure.

2.1. Glass-fiber reinforced polymer

Glass-fiber reinforced polymer (GRP) consists of a polymer matrix reinforced with thin glass fibers. Strong mechanical properties, i.e. high strength, are achieved when the glass fibers are free of defects. Full glass material without defects would have comparable strength, however, in contrast to glass fibers, it is practically impossible to build defect-free full glass materials. The main properties of GRP are light weight, extreme strength, and robustness. In comparison to carbon fiber reinforced polymers, the GRP has lower strength and is less stiff. Still, the GRP is typically far less brittle, and the raw materials are less expensive. A GRP is stiff and strong in tension and compression along the mean fiber alignment. In other directions, i.e. orthogonal to their principal axis, the glass fiber is neither stiff nor strong with respect to shear. Therefore, the orientation distribution of the fibers plays a centered role for its physical behavior.

Common uses of GRP include boats, automobiles, baths, hot tubs, water tanks, roofing, pipes, cladding and external door skins. Details are given in [1] or [2]. Figure (1a) shows the original gray value image of the glass fiber reinforced polymer sample, provided by R. Velthuis from the IVW in Kaiserslautern. The image was recorded by A. Rack and J. Goebbels at the synchrotron BESSY in Berlin with a pixel sampling of $3.5\,\mu\text{m}$. As shown in the surface rendering of the binarized image (figure 1b), fibers do exhibit some small level of curvature.

2.2. Analysis of the microstructure characteristics

The main geometrical and statistical characteristics of the fibrous microstructure, important for this study, are the volume fraction and the distri-

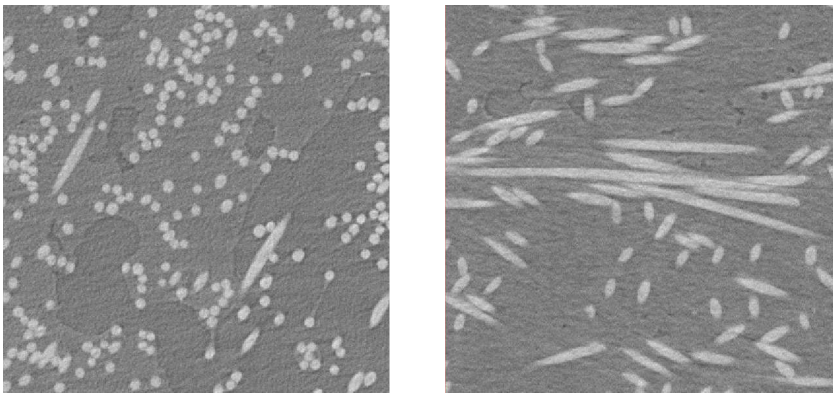

(a) 2D sections of the original gray-value image along the xy (left) and xz planes (right), shown at the same scale.

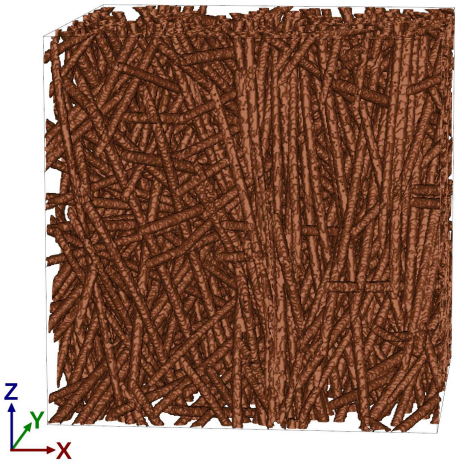

(b) Surface rendering of the binarized image.

Figure 1: GRP sample from R. Velthuis (IVW Kaiserslautern) recorded by A. Rack and J. Goebbels at the BAMline (BESSY II, Berlin, Germany) with a pixel sampling of 3.5 µm.

butions of the fiber orientations, radii, lengths and curvatures. Use is made of local analysis techniques to determine the fiber radius and orientation, that are directly applied on the gray value images [3]. Still, characteristics as lengths and curvature necessitate a fiber tracking approach, that makes it possible to follow the path of single fibers. In this respect, an algorithm for single fiber tracking is proposed in [4].

Figure 2 shows surface renderings of the reconstructed and labeled fibers versus the surface rendering of the original sample. Although most fibers are correctly reconstructed, it happens that fibers are split in two parts. This effect influences only the length estimation. Furthermore, the fact that most fibers extend over both boundaries of the image, complicates the length estimation. As such, most techniques used to estimate the average fibers length are not reliable, independently of the reconstruction. We measure the fiber volume fraction from the binarized image.

Figure 3 shows the length-weighted radius distribution from the separated fibers. The term length-weighted is to be understood as weighted statistics proportional to the fiber lengths, i.e. long fibers contribute more than short fibers. It is reminded that the number or length-weighted radius distribution is more accurate than the volume-weighted version [5], as the volume is dependent on the radius and therefore the volume-weighted radius distribution is distorted towards larger radii. The normal distribution $\mathcal{N}(5.44, 0.59)$ fits well to the numerically estimated radius distribution as shown in Figure 3.

Figure 4 shows the length-weighted orientation distribution of the fiber system on the unit sphere from two view angles. We observe a high probabil-

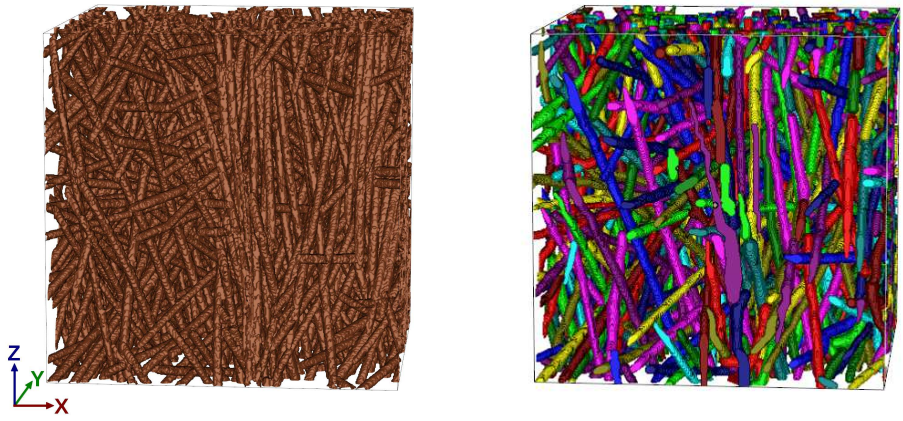

(a) Binary image. (b) Separated fibers.

Figure 2: Surface label renderings of the original binary image and the separated fibers.

ity of the direction along the z axis and a faint increase on a girdle passing the z axis. This distribution structure is fitted by a mixture of two β orientation distributions: one with preferred orientation close to the z axis and a second independent girdle distribution [6, section 8.3]. The β-distribution [7, 8] is a non-directed orientation distribution with one global parameter $\beta \in \mathbb{R}^+ \backslash \{0\}$. For $\beta = 1$ it results in the uniform distribution on the sphere, for $\beta \to 0$ the distribution concentrates on the z-axis and for $\beta \to \infty$ the orientations are distributed isotropically in the xy-plane.The probability density function of the β orientation distribution is

$$p(\theta, \phi \,|\, \beta) = \frac{\beta \sin\theta}{4\pi(1 + (\beta^2 - 1)\cos^2\theta)^{3/2}}. \tag{1}$$

where (θ, ϕ) are the polar coordinates of an orientation $\in S^2$. The final

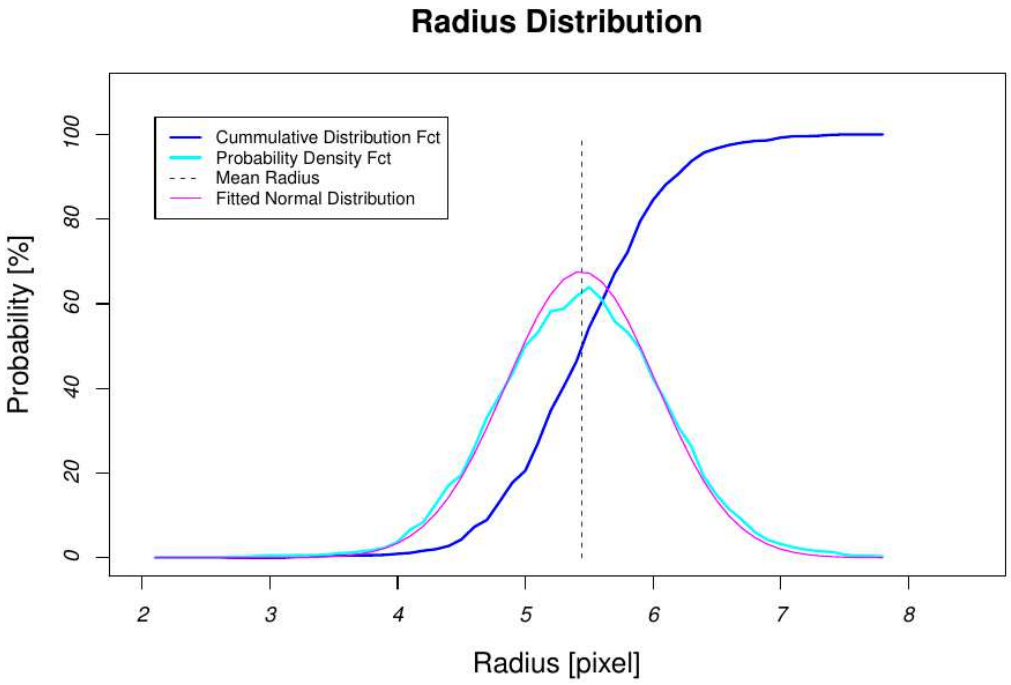

Figure 3: The empirical length-weighted radius distribution of the reconstructed fiber system and a fitted normal distribution $\mathcal{N}(5.44, 0.59)$.

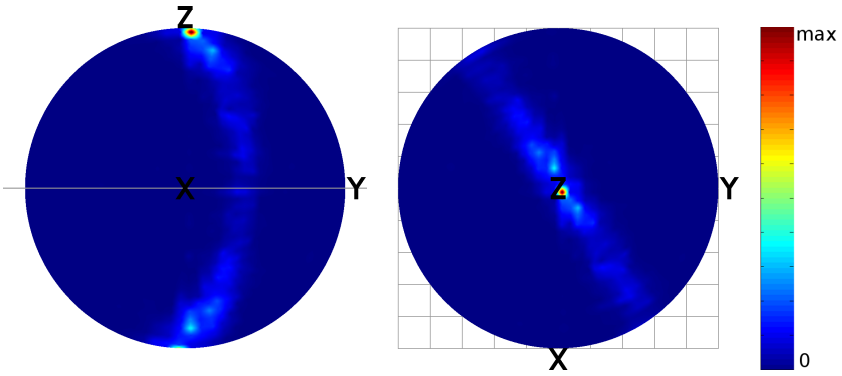

Figure 4: The empirical length weighted orientation distribution of the separated fiber system on the unit sphere. Accumulation near the z axis and on a girdle passing through the z pole is observed. The orientation distribution is given by the color scale density on the unit sphere, shown as stereographic projections from two different perspectives.

orientation distribution is estimated as:

$$P_{\beta\text{-mixed}}(\mu) = q_z P_\beta(\mu|\mu_z, \beta_z) + q_g P_\beta(\mu|\mu_g, \beta_g) \quad \text{with} \tag{2}$$

$$q_z = 0.393, \quad \mu_z = (0.075, -0.006, -0.997)^T, \quad \beta_z = 0.114 \tag{3}$$

$$q_g = 0.607, \quad \mu_g = (-0.526, 0.849, -0.045)^T, \quad \beta_g = 10.1. \tag{4}$$

Figure 5 shows a visualization of the mixed-β orientation distribution on the unit sphere.

Furthermore, the mean fiber length is estimated as 340 pixels (1.19 mm) according to the method proposed in [9], that approximates the mean fiber length by the lengths of the fiber parts and visible ends. The mean fiber length is most probably underestimated since, as the fiber tracking was not always completely successful in reconstructing the fiber with its full length. The fiber curvature is captured by the parameter of a stochastic model. We

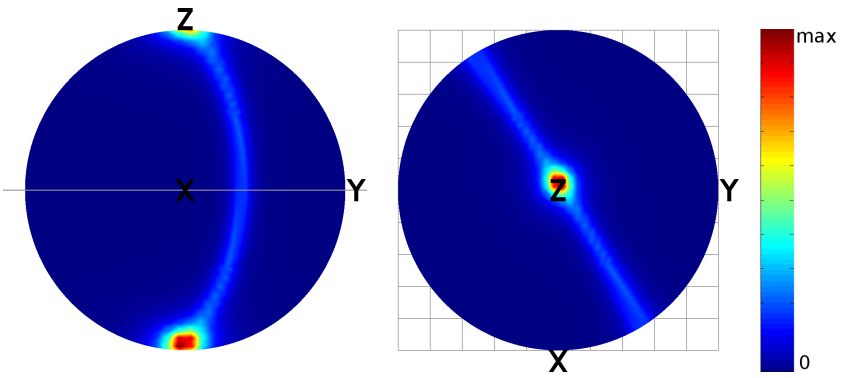

Figure 5: The fitted orientation distribution as a mixture of two β distributions presented in Equation (2).

assume that the fiber structure follows a random walk with a multivariate von Mises-Fisher orientation distribution [10, 11, 12, 13]. The parameters of this distribution are two preferred directions and their reliability parameters κ_1 and κ_2. In our case, the preferred directions are the main fiber orientation μ_1 and the last chosen orientation μ_{i-1}. The level of bending is defined by the reliability parameters. The probability density function for the orientation distribution of the i-th step in the random walk is

$$f(\mu_i|\mu_1, \kappa_1, \mu_{i-1}, \kappa_2) = c(\mu_1, \kappa_1, \mu_{i-1}, \kappa_2)\ e^{\kappa_1 \mu_1^T \mu_i + \kappa_2 \mu_{i-1}^T \mu_i}. \tag{5}$$

The factor $c(x_1, \kappa_1, x_2, \kappa_2)$ serves for the normalization, such that the integral over S^2 is equal to 1. The normalization factor is

$$c(x_1, \kappa_1, x_2, \kappa_2) = \frac{|\kappa_1 x_1 + \kappa_2 x_2|}{2\pi(e^{|\kappa_1 x_1 + \kappa_2 x_2|} - e^{-|\kappa_1 x_1 + \kappa_2 x_2|})}. \tag{6}$$

The curvature parameters are estimated in [9]: $\kappa_1 = 30.1612$ and $\kappa_2 = 109.077$. The parameter κ_1 is interpreted as the loyalty to the main fiber orientation or global straightness of the fiber, whereas κ_2 describes the local smoothness or straightness of the drift of the fiber core.

2.3. Stochastic model

Altendorf et al. [14] introduced a new stochastic model that generalizes the force-biased packing approach to fibers, represented as chains of spheres. This structure gives the fibers a flexible behavior during the packing process. The starting configuration is first modeled using random walks, where two parameters (κ_1 and κ_2) in the multivariate von Mises-Fisher orientation distribution control the bending. Adding an initial placement strategy to place the fibers at locations with minimal overlap reduces the computation time of the packing algorithm [15]. The final fiber configuration is obtained as an equilibrium between repulsion forces (avoiding crossing fibers) and recovering forces (ensuring a correct fiber structure). In the model, the fibers do not interpenetrate but contact is allowed. This approach provides for high volume fractions of up to 72%.

The parameters for the stochastic modeling are adapted to the real microstructure, as they are extracted from the previously described reconstructed fiber system. An overview of the parameters is presented in Table 1.

Additionally to the force-biased fiber packing, a Boolean cylinder model, where fibers are randomly placed using a Poisson point process, is considered with the same orientation characteristics except for the curvature. To study the influence of the microstructure on the physical behavior of the material, different parameter sets are tested for the orientation distribution and the fiber bending. We study three groups of microstructures and let one (or two) microstructural parameters vary in each group. In all microstructures, the fibers properties and volume fraction, their radius distribution and mean

Parameters	Values	Remarks
Vol. Fraction	$V_V = 15.01\%$	measured on the binarized image
Radius Distribution	$P_R = \mathcal{N}(5.44\,\text{pixels}, 0.59\,\text{pixels})$ $= \mathcal{N}(19.04\,\mu\text{m}, 2.065\,\mu\text{m})$	fitted normal distribution
Mean Length	$\widehat{L} = 340\,\text{pixels} = 1.19\,\text{mm}$	measured on separated fibers
Global, local straightness	$\widehat{\kappa_1} = 40$, $\widehat{\kappa_2} = 120$ (resp.)	
Orientation	$P_{\beta-\text{mixed}}(\mu)$ (see equation 2)	fitted distribution

Table 1: The model parameters estimated from the reconstructed fiber system or the binary image of the real material and used as input for the stochastic model.

length (and the aspect ratio) are fixed, as given in table (1). This leaves the orientation distribution and curvatures left to define. In the first group of microstructures, the fibers bending is fixed by $\widetilde{\kappa}_{1,2} = 40$, 120 and the fibers orientation follow a β-distribution, i.e. the microstructure are transverse isotropic with symmetry axis z. Increasing values of $\beta \geq 0$ are used to simulate different fiber orientations. The "z-preferred", isotropic and planar distributions are recovered when $\beta \ll 1$, $\beta = 1$ and $\beta \gg 1$ resp.

The second group of microstructures consist of a combination of two β-distributions oriented along μ_z and μ_g (see equation 2). The two distributions have weight q and $1-q$, resp., with varying q. Transverse isotropic orientation distributions are recovered when $q = 0$ or $q = 1$, whereas in general an orthotropic distribution is found when $0 < q < 1$. The fibers bending is fixed by the parameters $\widetilde{\kappa}_{1,2}$ so that the stochastic model fitted to the real material

is recovered when $q \approx 0.39$. Finally, the third group of microstructures consist in orthotropic distributions of fibers. Again, we use a combination of two β-distributions along μ_z and μ_g but with q fixed to $q \approx 0.39$. Increasing values of the straightness parameters κ_1 and κ_2 are considered to model the effect of fibers bending. Straight cylinders are found in the limit $\kappa_{1,2} \gg 1$. The stochastic model fitted to the real material is recovered when $\kappa_{1,2} = \widetilde{\kappa}_{1,2}$. For the first two groups of microstructures, we consider Boolean models of straight cylinders with the same geometrical parameters for the radiuses, mean length and orientation distribution, for comparison purpose. Some of the microstructures that belong in each group are shown in Figure 6.

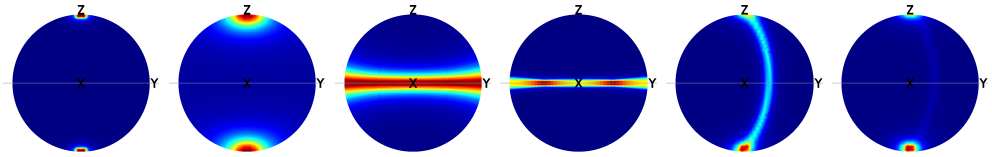

(a) Orientation distributions on the unit sphere

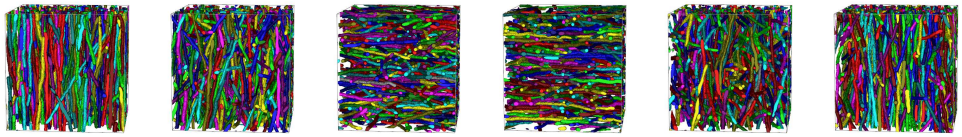

(b) Realizations of the orientation distributions in (a)

Figure 6: Variety of orientation distributions and their realizations. From left to right: transversely isotropic Z-pref. ($\beta = 0.05$), Z-pref. ($\beta = 0.3$), Planar ($\beta = 5$) and Planar ($\beta = 30$), and two orthotropic mixed-β distributions with $q = 0.2$ and $q = 0.8$.

3. Mechanical and thermal properties of a fibrous material

This section is devoted to the mechanical and thermal properties of fibrous materials, and to the underlying physical models adopted in this work.

Equations governing the local and overall elastic response of fibrous materials are given in section 3.1. The different types of microstructure anisotropy and the resulting forms of the macroscopic elastic tensor, in particular, are discussed in sections 3.1.1, 3.1.2 and 3.1.3. Section 3.2 addresses the thermal response of the materials. The materials properties are numerically solved by means of full-field FFT computations, which is recalled briefly in section 3.3. Section 3.4 reports the available analytical bounds for the effective properties and their relevance for different anisotropy cases. Finally, the representative volume element is defined in section 3.5.

3.1. Linear Elasticity

Under small deformation, we assume that the composite materials considered in this work follows the classical assumptions of micro-mechanics with linear elastic behavior [16, 17, 18, 19, 20, 21, 22]. The local stress and strain tensors $\widetilde{\sigma}(\mathbf{x})$ and $\widetilde{\varepsilon}(\mathbf{x})$ at point $\mathbf{x}$ are related by Hooke's law $\widetilde{\sigma}_{ij}(\mathbf{x}) = \widetilde{C}_{ij,kl}(\mathbf{x})\widetilde{\varepsilon}_{kl}(\mathbf{x})$ $(i,\ j,\ k,\ l = 1,\ ...,\ 3)$ where the local response of the material at point $\mathbf{x}$ is given by the 4^{th}-order stiffness tensor $\widetilde{C}_{ij,kl}(\mathbf{x})$. This tensor depends only on the phase at point $\mathbf{x}$, i.e. on the fiber or matrix constitutive laws. Under the hypothesis of small deformation, the local strain is expressed in terms of the local displacement vector $\mathbf{u}$ as

$$\widetilde{\varepsilon}(\mathbf{x}) = (1/2)[\partial_i u_j(\mathbf{x}) + \partial_j u_i(\mathbf{x})],$$

whereas stress equilibrium reads

$$\partial_i \widetilde{\sigma}_{ij}(\mathbf{x}) = 0,$$

where ∂_i is the derivative over x_i. Strain loading is applied on a volume Ω by means of periodic boundary conditions so that the overall strain $\varepsilon = \langle\widetilde{\varepsilon}(\mathbf{x})\rangle_\Omega$ is

prescribed. The effective response of the material is defined by the resulting overall stress $\sigma = \langle \widetilde{\sigma}(\mathbf{x}) \rangle_{\Omega}$. Here the overall stress and strain follow Hooke's law at the macroscopic scale as well, i.e.

$$\sigma_{ij} = C_{ij,kl}\varepsilon_{kl} \qquad \text{for } i,j,k,l \in \{x,y,z\}. \tag{7}$$

Accordingly, the stiffness tensor C_{ijkl} completely defines the material overall behavior. Due to the microstructure anisotropy, however, the tensor C_{ijkl} follows, in general, triclinic (i.e. full) anisotropy, which comprises 21 elastic moduli. In the Voigt notation [21]:

$$\begin{pmatrix} \sigma_{xx} \\ \sigma_{yy} \\ \sigma_{zz} \\ \sigma_{yz} \\ \sigma_{xz} \\ \sigma_{xy} \end{pmatrix} = \begin{pmatrix} C_{11} & C_{12} & C_{13} & C_{14} & C_{15} & C_{16} \\ C_{12} & C_{22} & C_{23} & C_{24} & C_{25} & C_{26} \\ C_{13} & C_{23} & C_{33} & C_{34} & C_{35} & C_{36} \\ C_{14} & C_{24} & C_{34} & C_{44} & C_{45} & C_{46} \\ C_{15} & C_{25} & C_{35} & C_{45} & C_{55} & C_{56} \\ C_{16} & C_{26} & C_{36} & C_{46} & C_{56} & C_{66} \end{pmatrix} \cdot \begin{pmatrix} \varepsilon_{xx} \\ \varepsilon_{yy} \\ \varepsilon_{zz} \\ \varepsilon_{yz} \\ \varepsilon_{xz} \\ \varepsilon_{xy} \end{pmatrix}, \tag{8}$$

where $(C_{rs})_{1 \leq r,s \leq 6}$ is a second-rank symmetrical tensor. Statistical symmetries related to particular microstructures reduce the number of independent components, as explained in detail in the following subsections. The stiffness matrix is numerically estimated by examining several strain loading directions ε and the resulting stress tensor σ. The following loading modes for the

strain tensor are considered:

$$\varepsilon^{C} = \begin{pmatrix} 1 & 0 & 0 \\ & 1 & 0 \\ & & 1 \end{pmatrix}, \quad \varepsilon^{S1} = \begin{pmatrix} 1 & 0 & 0 \\ & 1 & 0 \\ & & -2 \end{pmatrix}, \quad \varepsilon^{S1b} = \begin{pmatrix} 1 & 0 & 0 \\ & -2 & 0 \\ & & 1 \end{pmatrix}, \tag{9}$$

$$\varepsilon^{S2} = \begin{pmatrix} 0 & 1 & 0 \\ & 0 & 0 \\ & & 0 \end{pmatrix}, \quad \varepsilon^{S3} = \begin{pmatrix} 0 & 0 & 0 \\ & 0 & 1 \\ & & 0 \end{pmatrix}, \quad \varepsilon^{S4} = \begin{pmatrix} 0 & 0 & 1 \\ & 0 & 0 \\ & & 0 \end{pmatrix}. \tag{10}$$

The resulting stress tensors $\sigma^{C,S1,S1b,S2,S3,S4}$ give the full stiffness matrix C_{rs}, which is equivalently represented by the axis dependent Young's moduli E and Poisson's ratios ν, as well as the shear moduli G. The bulk modulus K is likewise extracted from $\sigma^{C,S1,S1b,S2,S3,S4}$. The latter is defined here as the ratio of mean stress $\sigma_m = (\sigma^C_{xx} + \sigma^C_{yy} + \sigma^C_{zz})/3$ to the relative volume change $\Delta V/V$, i.e.

$$K = \frac{\sigma_m}{\Delta V/V} = \frac{\sigma_m}{\varepsilon_{xx} + \varepsilon_{yy} + \varepsilon_{zz}} = \frac{\sigma^C_{xx} + \sigma^C_{yy} + \sigma^C_{zz}}{9}. \tag{11}$$

3.1.1. Isotropy

In isotropic media, the elasticity tensor is invariant by rotations of the coordinate system. It is reminded that fibrous materials are isotropic whenever the fiber orientations are isotropically distributed. In that simple case, the stiffness matrix reduces to two independent scalars C_{11} and C_{44}, as shown in equation (12) with $C_{11} = \frac{E(1-\nu)}{(1+\nu)(1-2\nu)}$ and $C_{44} = \frac{E}{(1+\nu)}$ as diagonal elements.

The non-diagonal values are equal to $C_{11} - C_{44}$ or zero as shown below

$$C_{rs} = \begin{pmatrix} \mathbf{C_{11}} & C_{11}\text{-}C_{44} & C_{11}\text{-}C_{44} & 0 & 0 & 0 \\ C_{11}\text{-}C_{44} & \mathbf{C_{11}} & C_{11}\text{-}C_{44} & 0 & 0 & 0 \\ C_{11}\text{-}C_{44} & C_{11}\text{-}C_{44} & \mathbf{C_{11}} & 0 & 0 & 0 \\ 0 & 0 & 0 & C_{44} & 0 & 0 \\ 0 & 0 & 0 & 0 & C_{44} & 0 \\ 0 & 0 & 0 & 0 & 0 & C_{44} \end{pmatrix}. \tag{12}$$

Accordingly, it is sufficient to apply two strain loading modes, compression ε^C and shear strain defined as

$$\varepsilon^S = \varepsilon^{S2} + \varepsilon^{S3} + \varepsilon^{S4} = \begin{pmatrix} 0 & 1 & 1 \\ & 0 & 1 \\ & & 0 \end{pmatrix}. \tag{13}$$

The resultant stress tensors σ^C and σ^S simplify to $\sigma_m = \frac{\sigma^C_{xx}+\sigma^C_{yy}+\sigma^C_{zz}}{3}$ and $\sigma_d = \frac{\sigma^S_{xy}+\sigma^S_{yz}+\sigma^S_{xz}}{3}$, from which the elastic moduli are computed as follows:

$$\nu = \frac{\sigma_m - \sigma_d}{2\sigma_m - \sigma_d}, \quad E = \sigma_d(1+\nu), \quad \text{and} \quad G = \frac{\sigma_d}{2}. \tag{14}$$

3.1.2. Transverse Isotropy

For a transversely isotropic microstructure, the stiffness matrix simplifies to 5 independent values. Assuming the latter is the z-axis, the material properties do not change under rotation around the z-axis. Accordingly, the material is statistically isotropic along planes orthogonal to z. This is in particular true for fiber systems with the β distribution as global fiber

orientation distribution. In this situation, Hooke's Law reads

$$C_{rs} = \begin{pmatrix} \frac{1-\nu_{pz}\nu_{zp}}{E_pE_z\Delta} & \frac{\nu_p+\nu_{pz}\nu_{zp}}{E_pE_z\Delta} & \frac{\nu_{zp}+\nu_p\nu_{zp}}{E_pE_z\Delta} & 0 & 0 & 0 \\ \frac{\nu_p+\nu_{pz}\nu_{zp}}{E_pE_z\Delta} & \frac{1-\nu_{pz}\nu_{zp}}{E_pE_z\Delta} & \frac{\nu_{zp}+\nu_p\nu_{zp}}{E_pE_z\Delta} & 0 & 0 & 0 \\ \frac{\nu_{pz}+\nu_p\nu_{pz}}{E_p^2\Delta} & \frac{\nu_{pz}(1+\nu_p)}{E_p^2\Delta} & \frac{1-\nu_p^2}{E_p^2\Delta} & 0 & 0 & 0 \\ 0 & 0 & 0 & 2G_{zp} & 0 & 0 \\ 0 & 0 & 0 & 0 & 2G_{zp} & 0 \\ 0 & 0 & 0 & 0 & 0 & \frac{E_p}{1+\nu_p} \end{pmatrix}, \quad (15)$$

with $\Delta = \frac{(1+\nu_p)(1-\nu_p-2\nu_{pz}\nu_{zp})}{E_p^2E_z}$. The 5 engineering constants in the stiffness matrix are the "parallel" and "transverse" Young's modulus E_z and E_p, along the z axis and xy plane, Poisson's ratios ν_p and ν_{pz} and the shear modulus G_{zp} [23]. Poisson's ratio ν_{zp} is related to ν_{pz} by $\nu_{pz}/E_p = \nu_{zp}/E_z$. The four strain loading modes $\varepsilon^{C,S1,S2,S3}$ are sufficient to compute C_{rs}:

$$\begin{aligned} C_{44} &= \sigma_{yz}^{S3}, \quad C_{33} = \frac{\sigma_{zz}^{C} - \sigma_{zz}^{S1}}{3}, \quad C_{13} = \frac{\sigma_{xx}^{C} - \sigma_{xx}^{S1}}{3} \\ C_{11} &= \frac{1}{3}\sigma_{xx}^{C} + \frac{1}{6}\sigma_{xx}^{S1} + \frac{1}{2}\sigma_{xy}^{S2}, \quad C_{12} = \frac{1}{3}\sigma_{xx}^{C} + \frac{1}{6}\sigma_{xx}^{S1} - \frac{1}{2}\sigma_{xy}^{S2}. \end{aligned}$$

Or equivalently:

$$\begin{aligned} G_{zp} &= \frac{1}{2}C_{44}, \quad \nu_{zp} = \frac{C_{13}}{C_{11}+C_{12}}, \quad \nu_p = \frac{E_p}{C_{11}-C_{12}} - 1, \\ E_z &= C_{33} - \frac{2C_{13}^2}{C_{11}+C_{12}}, \quad E_p = \frac{(C_{11}-C_{12})\left[C_{33}(C_{11}+C_{12}) - 2C_{13}^2\right]}{C_{11}C_{33} - C_{13}^2}. \end{aligned}$$

3.1.3. Orthotropic Materials

A material is orthotropic if its mechanical and thermal properties are described by three perpendicular axes. The classic example for orthotropy is a partial cutout of wood. The three axes of wood are: the fiber directions,

the direction tangential to visual part of the growth rings and the direction normal to the growth rings. This example yields only for a wood panel. A slice of wood with the complete growth rings would be transversely isotropic. In particular, fiber-reinforced materials are orthotropic when the fiber orientation distribution is a combination of two β distributions oriented along orthogonal axes. In the case of orthotropic materials, the stiffness matrix is described by 9 values as follows:

$$C_{rs} = \begin{pmatrix} C_{11} & C_{12} & C_{13} & 0 & 0 & 0 \\ C_{12} & C_{22} & C_{23} & 0 & 0 & 0 \\ C_{13} & C_{23} & C_{33} & 0 & 0 & 0 \\ 0 & 0 & 0 & C_{44} & 0 & 0 \\ 0 & 0 & 0 & 0 & C_{55} & 0 \\ 0 & 0 & 0 & 0 & 0 & C_{66} \end{pmatrix}. \tag{16}$$

For the computation of the stiffness matrix C_{rs}, all 6 strain modes as described in Equation (10) are required. The values C_{rs} of the stiffness matrix are given by

$$C_{44} = \sigma_{yz}^{S3} \qquad C_{13} = \frac{\sigma_{xx}^{C} - \sigma_{xx}^{S1}}{3} \qquad C_{12} = \frac{\sigma_{xx}^{C} - \sigma_{xx}^{S1b}}{3} \tag{17}$$

$$C_{55} = \sigma_{xz}^{S4} \qquad C_{23} = \frac{\sigma_{yy}^{C} - \sigma_{yy}^{S1}}{3} \qquad C_{22} = \frac{\sigma_{yy}^{C} - \sigma_{yy}^{S1b}}{3} \tag{18}$$

$$C_{66} = \sigma_{xy}^{S2} \qquad C_{33} = \frac{\sigma_{zz}^{C} - \sigma_{zz}^{S1}}{3} \qquad C_{11} = \frac{\sigma_{xx}^{C} + \sigma_{xx}^{S1} + \sigma_{xx}^{S1b}}{3}. \tag{19}$$

The inverse of the stiffness matrix, known as the compliance matrix, is described by

$$C_{rs}^{-1} = \begin{pmatrix} \frac{1}{E_x} & -\frac{v_{xy}}{E_x} & -\frac{v_{xz}}{E_x} & 0 & 0 & 0 \\ -\frac{v_{xy}}{E_x} & \frac{1}{E_y} & -\frac{v_{yz}}{E_y} & 0 & 0 & 0 \\ -\frac{v_{xz}}{E_x} & -\frac{v_{yz}}{E_y} & \frac{1}{E_z} & 0 & 0 & 0 \\ 0 & 0 & 0 & \frac{1}{2G_{yz}} & 0 & 0 \\ 0 & 0 & 0 & 0 & \frac{1}{2G_{zx}} & 0 \\ 0 & 0 & 0 & 0 & 0 & \frac{1}{2G_{xy}} \end{pmatrix}. \tag{20}$$

In particular, the lower right part leads directly to the following relations:

$$G_{yz} = \frac{1}{2}C_{44}, \quad G_{zx} = \frac{1}{2}C_{55}, \quad G_{xy} = \frac{1}{2}C_{66} \tag{21}$$

By inverting the upper-left part of the stiffness matrix C_{rs}, the following relations are found:

$$E_x = \frac{D}{C_{22}C_{33} - C_{23}^2} \qquad v_{xy} = -E_x \frac{C_{13}C_{23} - C_{12}C_{33}}{D} \tag{22}$$

$$E_y = \frac{D}{C_{11}C_{33} - C_{13}^2} \qquad v_{xz} = -E_x \frac{C_{12}C_{23} - C_{13}C_{22}}{D} \tag{23}$$

$$E_z = \frac{D}{C_{11}C_{22} - C_{12}^2} \qquad v_{yz} = -E_y \frac{C_{13}C_{12} - C_{23}C_{11}}{D} \tag{24}$$

with $D = C_{11}C_{22}C_{33} + 2C_{12}C_{13}C_{23} - C_{11}C_{23}^2 - C_{22}C_{13}^2 - C_{33}C_{12}^2$.

Inversely, assumptions of orthotropy, transverse isotropy or isotropy are verified, in terms of the material response, by inspecting the complete stiffness matrix. This necessitates numerical computations for at least 6 loading modes, for which the strain tensors are linearly independent. With the 6 resulting stress tensors, all 21 values of C_{rs} of the stiffness matrix can be reconstructed and symmetries verified.

3.2. Linear Thermal Conductivity

For steady-state conduction, the material local thermal behavior is defined by Fourier's law $\widetilde{q}_i(\mathbf{x}) = \widetilde{k}(\mathbf{x})\widetilde{E}_i(\mathbf{x})$ where $\widetilde{k}(\mathbf{x})$ is the phase-dependent thermal conductivity (measured in Watt per meter Kelvin), $\widetilde{E}(\mathbf{x}) = -\partial_i T(\mathbf{x})$ is the opposite of the temperature gradient (measured in Kelvin per meter), and $\widetilde{q}(\mathbf{x})$ is the heat flux vector (measured in Watt per square meter). Heat flux conservation reads $\partial_i \widetilde{q}_i(\mathbf{x}) \equiv 0$. As in the elastic case, periodic boundary conditions are applied so that a macroscopic temperature gradient is prescribed over a volume Ω, i.e. $E = \langle \widetilde{E}(\mathbf{x}) \rangle_\Omega$ is given. The overall heat flux $q = \langle \widetilde{q}(\mathbf{x}) \rangle_\Omega$ is linearly related to E as $q_i = k_{ij} E_j$ where the anisotropic second-rank tensor $\mathbf{k}$ completely defines the macroscopic thermal behavior of the microstructure.

For the isotropic and anisotropic fibrous media considered here, the conductivities k is represented in the (x, y, z) axes as a diagonal tensor. In the isotropic case, all principal values k_{ii} are equal. In the case of transverse isotropy around the z axis, the conductivity in the x and y directions are equal: $k_{11} = k_{22} = k_p$ and differs from that in the z direction $k_{33} = k_z$. In the orthotropic case, all directions are treated separately: $k_{ii} \neq k_{jj}$ if $i \neq j$. A macroscopic temperature gradient is applied over the samples so that E is set to:

$$E^{C1} = \begin{pmatrix} 1 \\ 0 \\ 0 \end{pmatrix}, \qquad E^{C2} = \begin{pmatrix} 0 \\ 1 \\ 0 \end{pmatrix}, \quad \text{and} \quad E^{C3} = \begin{pmatrix} 0 \\ 0 \\ 1 \end{pmatrix}. \tag{25}$$

In the case of transverse isotropy, it is sufficient to consider the applied temperature difference E^{C3} and any of E^{C1} or E^{C2}, whereas, for isotropic

media, $E^{C1,C2,C3}$ are statistically equivalent.

It is noted that the linear constitutive laws considered above, discussed in the context of thermal conductivity, apply to other mathematically-equivalent problems such as thermal conductivity.

3.3. Full-field Fourier-based computations

The local and apparent macroscopic elastic and thermal fields of the fibrous realizations are readily determined using the Fast Fourier transform method [24, 25]. The method has been applied successfully to compute the mechanical response of composites and is not limited to materials with linear responses [26, 27]. The so-called accelerated scheme algorithm [28], particularly efficient to treat highly contrasted composites, is used, thanks to the software Morph'Hom [29, 30], developed at the Center of Mathematical Morphology in Fontainebleau. This image-based numerical method does not necessitate prior meshing; equilibrium or heat flux conservation are, in particular, treated locally in the Fourier domain. Binary images are seen as the elementary cell Ω of a periodic microstructure, accordingly to the Fourier representation. More precisely, stress equilibrium (resp. heat flux conservation) is enforced along the cell boundary $\partial\Omega$, so that $\sigma \cdot \mathbf{n}$ (resp. $\mathbf{q} \cdot \mathbf{n}$) is anti-periodic, where $\mathbf{n}$ is the normal along the boundary $\partial\Omega$ directed outward. Macroscopic loading conditions are applied so that the overall deformation $\langle \widetilde{\varepsilon}(\mathbf{x}) \rangle_\Omega$ (resp. the mean temperature gradient field $\langle \widetilde{E}(\mathbf{x}) \rangle_\Omega$) are prescribed by setting, in the Fourier domain, $FFT\left(\widetilde{\varepsilon}; \mathbf{r} = 0\right) = \varepsilon$ and $FFT\left(\widetilde{E}; \mathbf{r} = 0\right) = E$ where $\mathbf{r}$ is the wave-vector.

3.4. Bounds for the effective mechanical and thermal properties

Numerical results are compared with the well-known Hashin and Shtrikman bounds [31, 32], hereafter referred to as HS bounds:

$$\begin{aligned}
K - c_1K_1 - c_2K_2 &\leq \frac{-c_1c_2(K_1-K_2)^2}{c_2K_1 + c_1K_2 + (2-2/d)G_1}, \\
&\geq \frac{-c_1c_2(K_1-K_2)^2}{c_2K_1 + c_1K_2 + (2-2/d)G_2}, \\
G - c_1G_1 - c_2G_2 &\leq \frac{-c_1c_2(G_1-G_2)^2}{c_2G_1 + c_1G_2 + [dK_1/2 + (4-8/d)G_1]/(2+K_1/G_1)}, \\
&\geq \frac{-c_1c_2(G_1-G_2)^2}{c_2G_1 + c_1G_2 + [dK_2/2 + (4-8/d)G_2]/(2+K_2/G_2)}, \\
k_2 + \frac{dc_1k_2}{dk_2 + c_2(k_1-k_2)} &\leq k \leq k_1 + \frac{dc_2k_1}{dk_1 + c_1(k_2-k_1)}
\end{aligned}$$

where $d = 2,\ 3$ is the dimension, $c_1 = 15\%$ is the fiber volume fraction and $c_2 = 1 - c_1$. In elasticity, these bounds extend to Young's modulus (in 2D and 3D) and Poisson's ratio (in 3D) with:

$$E = \left[\frac{1}{d^2K} + \frac{1}{(6-d)G}\right]^{-1}, \qquad \nu = \frac{3K-2G}{2(3K+G)}.$$

The 3D HS bounds apply to isotropic distributions of fibers only. For arbitrary fiber distributions, the broader Reuss and Voigt bounds in elasticity and the Wiener bounds in conductivity, i.e. the geometric and arithmetic phase properties average, hold. For comparison purpose, we also consider the 2D Hashin and Shtrikman bounds, appropriate to plane strain problems and the (3D) self-consistent estimates. The self-consistent bulk and shear moduli K^* and G^* are the solutions of [33]:

$$\sum_{j=1}^{2} \frac{c_j(K_j - K^*)}{K_j - 4G^*/3} = \sum_{j=1}^{2} \frac{c_j(G_j - G^*)}{G_j + G^*[(3/2)K^* + (4/3)G^*]/(K^* + 2G^*)} = 0,$$

whereas in conductivity we solve:

$$\sum_{j=1}^{2} c_j \frac{k_j - k^*}{k_j + 2k^*} = 0.$$

3.5. Representative Volume Element

The representative volume element (RVE) is a volume of "minimal" size that exhibits a behavior "representative" for a real microstructure. Consider a local (elastic or thermal) field $Z(\mathbf{x})$ and its mean over V, $\bar{Z} = \langle Z(\mathbf{x}) \rangle_V = (1/V) \int_V Z(\mathbf{x}) \mathrm{d}\mathbf{x}$. The variance of the random variable $\bar{Z}$ is given by

$$D_Z^2(V) = \frac{D_Z^2(1)\ A_3^\alpha}{V^\alpha}, \quad V \gg A_3 \tag{26}$$

where $D_Z^2(1) = \langle Z(\mathbf{x})^2 \rangle_V - \bar{Z}^2$ is the point variance, A_3 is the integral range in 3D, and $\alpha \leq 1$. The quantity $D_Z^2(V)$ is estimated by computing the mean of the field $Z(\mathbf{x})$ over m independent samples of size V [34, 35, 36] as follows

$$D_Z^2(V) = \frac{1}{m} \sum_{i=1}^{m} (\langle Z(\mathbf{x}) \rangle_{V_i} - \bar{Z})^2. \tag{27}$$

This approach allows one to verify that the scaling relation given in equation (26) applies in a range of volume sizes V, much larger than A_3 so that the number of subvolumes is large enough to compute a variance. Note that in materials with *finite* correlation lengths, $\alpha = 1$. This relation breaks down when considering degenerate microstructures with *infinite* correlation lengths [37], resulting in much larger RVE sizes. In this respect, $\alpha = 2/3$ for the scaling law of the volume fraction of Boolean varieties of infinite fibers [37]. Accordingly, we expect non-integer values of α as well for the mechanical effective properties of our fibrous microstructures.

The volume V is chosen so that $\bar{Z}$ is a good estimate of the effective response for stress or heat flux of the material. The relative error ϵ_{rel} and the absolute error ϵ_{abs} on the effective property $\bar{Z}$ depend on the sample volume V of n independent realizations by

$$\epsilon_{\text{rel}} = \frac{\epsilon_{\text{abs}}}{\bar{Z}} = \frac{2D_Z(V)}{\bar{Z}\sqrt{n}} \tag{28}$$

At a given relative error ϵ_{rel} (typically 1%), the RVE size is

$$V_{\text{RVE}} = \left(\frac{4\ D_Z^2\ A_3^\alpha}{\epsilon_{\text{rel}}^2\ \bar{Z}^2\ n} \right)^{1/\alpha}. \tag{29}$$

The choice of $Z(\mathbf{x})$ is driven by the physical property one wish to consider. For instance, when hydrostatic strain loading is applied, Z is set to the mean stress component σ_m, so that $\bar{Z}$ is, up to a constant, an estimate of the macroscopic bulk modulus. More generally, one would choose $Z(\mathbf{x})$ equal to the energy density in the system. Local fluctuations are induced by the microstructure and by the contrast of properties between the phases, as well as on the boundary conditions. In that respect, the use of periodic boundary conditions is known to minimize the RVE size compared to traditional kinematic or static uniform boundary conditions, as used in finite element computations [35].

4. Simulation results: elastic and thermal responses

In this section, results for the elastic and thermal responses of the stochastic models and of the original segmented material are given. Computations are based on binarizations of the microstructures. The mechanical and thermal properties for the fibers and surrounding matrix are given in Table 2.

The effective properties of the different microstructures are determined by the full-field results computed by the FFT method, as discussed in Section 3.3. Furthermore, the results are compared to the theoretical Hashin-Shtrikman, Reuss-Voigt and Wiener bounds. The size of the representative volume element (RVE) is finally computed for a cubic, elongated or flat window.

	Young's Modulus	Poisson's Ratio	Bulk Modulus	Shear Modulus	Thermal Conductivity
	$\widetilde{E}$ [MPa]	$\widetilde{\nu}$	$\widetilde{K}$ [MPa]	$\widetilde{G}$ [MPa]	$\widetilde{k}$ [W/mK]
Glass Fibers	72000	0.22	42857	29508	1
Polymer Matrix	2002	0.39	3033	720	0.2

Table 2: Elastic moduli and thermal conductivity of glass fibers and surrounding polymer matrix, from [36].

Examples of the elastic local fields computed by the FFT method are shown in Figure 7. The latter represent four 2D maps of the mean stress component σ_m and of the stress component $\sigma_{xx} - \sigma_{yy}$, cut along the (x, y) plane, for two isotropic and transversely isotropic fibrous models (top and bottom, respectively). The component $\sigma_{xx} - \sigma_{yy}$, transverse to the applied loading, exhibits heterogeneous local stress depending on the fibers orientation (unsurprisingly, positive if the fibers are directed parallel to the x direction, negative in the y direction, as seen in the top and bottom right maps). Fluctuations inside the fibers are most visible in the maps for the mean stress field σ_m (top and bottom left), parallel to the applied loading. More precisely, the mean stress field is highest along a fiber at places crossing or close to another fiber, a feature reminiscent of previous observations

in granular media [38].

4.1. Anisotropy of the stochastic model responses

In the numerical computations, the orthotropic, transversely isotropic and isotropic behaviors of the various fibrous microstructures are only conveyed approximately, due to finite-size effects. In this section, the deviation of the stiffness matrix with respect to the symmetries of the ideal isotropic models is evaluated. Optimally, the matrices fulfill the symmetries described in Section 3.1. First, for one arbitrarily chosen realization of the isotropic orientation distribution, the following stiffness matrix is found:

$$C_{\text{isotropic}} = \begin{pmatrix} 6391.44 & 3394.00 & 3365.64 & -28.85 & 46.35 & -26.38 \\ 3399.60 & 6502.43 & 3436.42 & -105.23 & -3.08 & -55.95 \\ 3378.52 & 3445.55 & 6394.85 & -121.69 & 28.27 & -12.45 \\ -60.56 & -216.24 & -243.37 & 3118.67 & -26.98 & -14.06 \\ 95.22 & -9.02 & 57.00 & -27.72 & 3053.90 & -79.30 \\ -56.45 & -114.16 & -24.90 & -14.06 & -76.42 & 3072.67 \end{pmatrix}. \quad (30)$$

This is to be compared with the form (12) of the matrix in the isotropic case, which depends on two parameters (section 3.1.1). The absolute of the values expected to be zero do not overrun 250, which is less than 8% of the smallest value on the diagonal. The diagonal values are not independent and match the isotropic symmetries up to small corrections. The mean of non-diagonal values in the top-left quarter is 3403.29, which is close to the difference of the mean of C_{11} and C_{44}: 3347.83. Accordingly, all symmetries for the simulated isotropic material are respected up to a relatively small deviation.

Second, two randomly chosen microstructure realizations, one having transverse isotropy with axis of rotation along z and one generated using

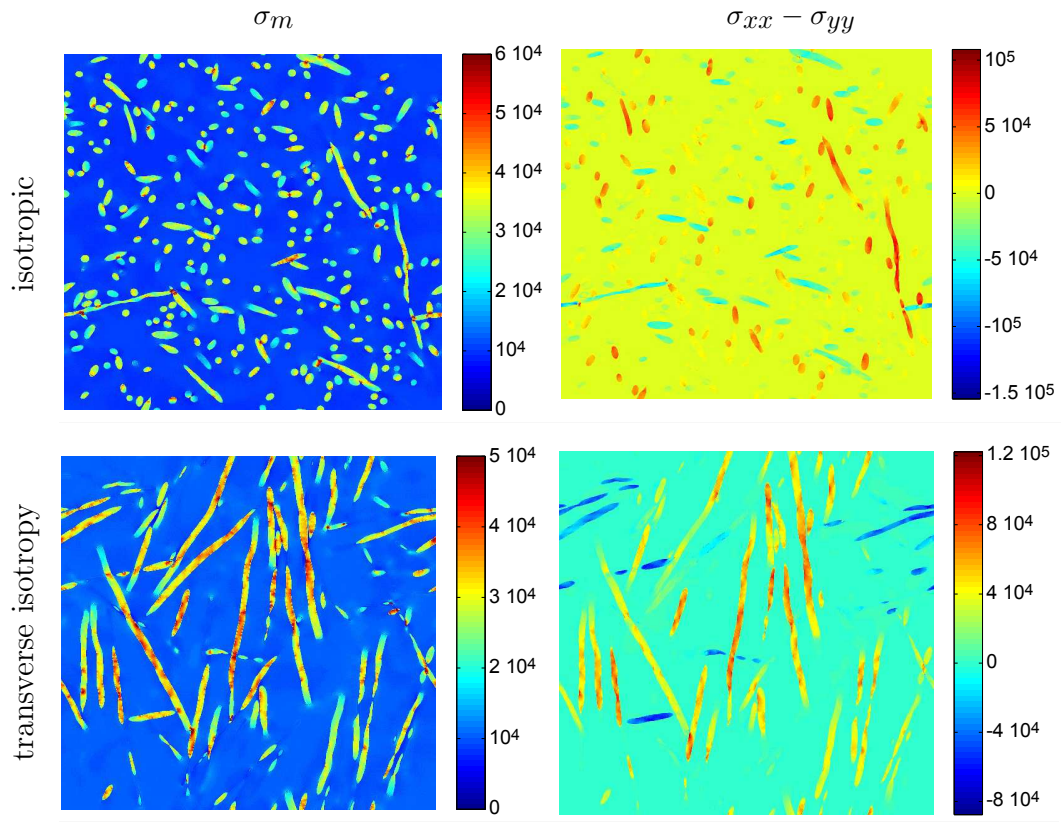

Figure 7: 2D sections along the (x, y) plane of the mean stress field $\sigma_m(\mathbf{x})$ (left) and of the stress component $\sigma_{xx}(\mathbf{x}) - \sigma_{yy}(\mathbf{x})$ (right) in fibrous microstructure models with isotropic (top) and transversely isotropic (bottom) distribution of fibers; hydrostatic strain loading with $\langle \varepsilon_m(\mathbf{x}) \rangle = 1$ is applied. The mean stress components have been thresholded to highlight the fields structure.

a girdle orientation distribution (see equation 15), are considered. The corresponding stiffness matrices are

$$C_{z\text{-preferred}} = \begin{pmatrix} 5179.43 & 2982.40 & 3141.73 & 1.74 & -1.74 & -1.91 \\ 3016.38 & 5031.73 & 3051.98 & -1.56 & -15.69 & -3.59 \\ 3090.30 & 3047.32 & 11227.94 & 0.84 & 31.92 & 2.49 \\ 3.77 & -3.22 & 0.46 & 2344.22 & 1.90 & -30.44 \\ -5.24 & -31.39 & 69.54 & 1.58 & 2466.12 & 3.94 \\ -0.91 & -7.18 & 4.13 & -31.88 & 3.94 & 2061.38 \end{pmatrix} \quad (31)$$

and

$$C_{\text{girdle}} = \begin{pmatrix} 7799.50 & 3780.97 & 2972.98 & -0.92 & 6.37 & 12.02 \\ 3780.97 & 7554.32 & 2975.42 & -13.65 & 2.03 & 37.79 \\ 2972.63 & 2974.84 & 5078.91 & -7.09 & -3.53 & 1.22 \\ -1.44 & -28.11 & -14.18 & 2169.46 & 5.12 & -1.06 \\ 13.37 & 3.39 & -7.06 & 5.12 & 2181.00 & 5.45 \\ 23.42 & 75.01 & 1.81 & -0.62 & 5.40 & 3820.53 \end{pmatrix}. \quad (32)$$

The highest value among the ones which ideally vanish in equation (15) is 75, which is less than 4% compared to all other non-vanishing values. The symmetry in x and y directions is approximately given as well. The equality of the lower right value to $C_{11} - C_{12}$ remains to be checked. The stiffness matrix for the z preferred orientations yields $C_{11} - C_{12} = 2197.03$ versus $C_{33} = 2061.38$ and for the girdle orientation, it yields $C_{11} - C_{12} = 4018.53$ versus $C_{33} = 3820.53$. Both results show a relatively small discrepancy of less than 5%. Accordingly, the transverse isotropy for the simulated material with single β distributions (either aligned or planar) is verified.

Finally, for general orthotropic microstructures, it is sufficient to verify that the values in the upper-right and lower-left quarters of the stiffness matrix as well as outside of the diagonal in the lower-right quarter, are small compared to the rest (equation 16). For an arbitrary realization of an orthotropic type microstructure it is found that

$$C_{\text{ortho}} = \begin{pmatrix} 6066.10 & 3348.66 & 3404.30 & 1.66 & -25.59 & 524.42 \\ 3360.65 & 5405.84 & 3210.74 & 35.35 & 8.05 & 228.07 \\ 3404.30 & 3202.34 & 8538.99 & 139.00 & -128.68 & 191.09 \\ 3.33 & 66.74 & 277.99 & 2652.07 & 403.67 & 6.86 \\ -51.19 & 15.67 & -257.37 & 403.67 & 3081.05 & 13.26 \\ 1026.54 & 430.45 & 373.77 & 6.29 & 12.84 & 2823.16 \end{pmatrix}. \tag{33}$$

Furthermore, the stiffness matrix of the original microstructure reads

$$C_{\text{orig}} = \begin{pmatrix} 5933.17 & 3283.14 & 3541.18 & 4.87 & -55.50 & 445.01 \\ 3283.14 & 5326.58 & 3210.82 & 28.35 & 26.48 & 190.44 \\ 3509.92 & 3197.54 & 8994.90 & 59.21 & -186.21 & 320.97 \\ 7.66 & 53.62 & 121.16 & 2733.97 & 697.23 & 35.24 \\ -107.38 & 48.60 & -372.41 & 683.03 & 3376.96 & 5.86 \\ 859.89 & 366.84 & 655.95 & 35.24 & 6.89 & 2709.74 \end{pmatrix}. \tag{34}$$

The highest value in places where elastic moduli of orthotropic media vanish is 1026.54. This value is not comparatively much smaller than the others. However, as there are only few outliers in the part, that is supposed to vanish, we still treat the material under conditions of orthotropic symmetry. The physical responses will be treated as approximations of the effective properties.

4.2. Representative Volume Element

The Representative Volume Element (RVE), introduced in section 3.5, is computed for various physical properties on realizations of the fiber model. Three types of orientation distributions are considered: z-preferred ($\beta = 0.05$), isotropic ($\beta = 1$) and planar ($\beta = 30$). Realizations of the stochastic model for cubic images with a volume of 600^3 pixels are used, with parameters of the models given in table 1. Periodic boundary conditions are applied. It is reminded that the mean values of the elastic or thermal fields over a volume give the apparent properties of the considered size. The variance of such mean values over non-overlapping subvolumes is computed at increasing volume sizes. As a complement to cubic RVEs, we also make use of RVEs with elongated (or shortened) cuboidal shapes of the form $\ell_x \times \ell_y \times \ell_z$ with $\ell_x = \ell_y$ and either $\ell_{x,y}/\ell_z = 10$ ("plate" shape) or $\ell_{x,y}/\ell_z = 0.1$ ("long" shape), which respect the transverse anisotropy of the fibers arrangement. Such forms allow to increase the statistics (or representativeness) in the x and y plane at the expense of that in the z direction and vice-versa, and to improve on the precision of the elastic moduli and thermal conductivity.

The variance $D_Z^2(V)$ of the apparent elastic moduli and thermal conductivity $\langle Z \rangle_V$ are first computed in subdomains of volume V. A powerlaw $\sim 1/V^\alpha$ is fitted with respect to the subvolume size $V \gg A_3$. An example is show in figure (8) for the bulk modulus K and z-preferred orientation distribution ($\beta = 0.05$), where the variance is represented as a function of the volume V in log-log scale. A region of interest is selected. On the one hand, the powerlaw is not valid for small ($\ll A_3$) volume sizes. On the other hand, the precision of the variance deteriorates for large volumes due to a small

number of configurations (8 for the larger sizes). To estimate the precision of the parameters of the fitted law, three regions of interest are manually selected in figure 8 resulting in three fitted laws. The resulting RVEs differ from 381^3 to 482^3 voxels. Likewise, the fitted exponent α varies but is close to 0.8. The variation in the exponent and RVE size estimates are, according to the theoretical constraints outlined above, an effect of the relatively small observation window of less than two decades. Improved precision should be achieved with either larger sizes or a higher number of realizations.

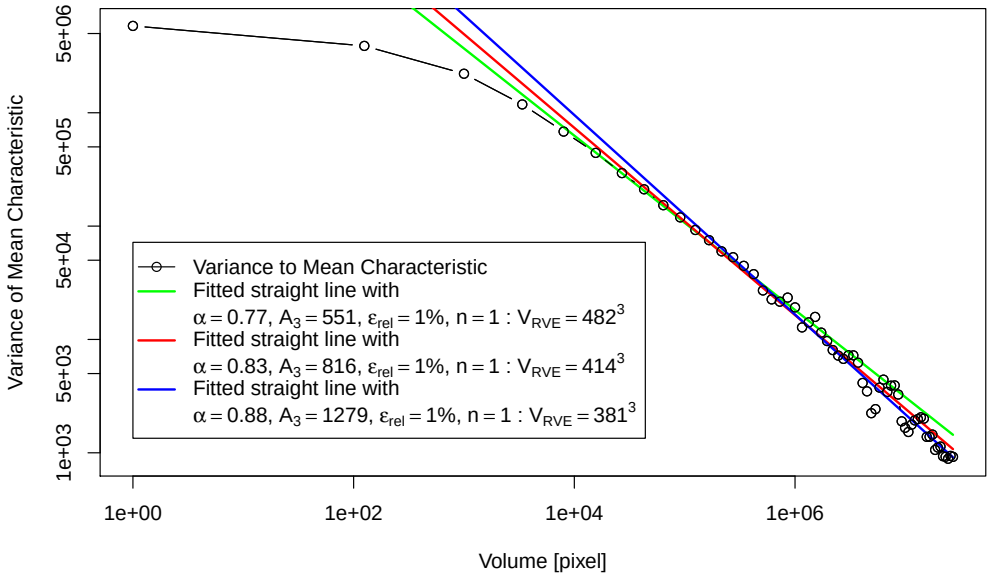

Figure 8: RVE sizes for the bulk modulus K in a fibrous microstructure with z-preferred orientation distribution ($\beta = 0.05$): variances of the apparent bulk modulus K vs. volume size computed from FFT data. Solid lines: numerical fits by a powerlaw $\sim 1/V^{\alpha}$. The three fits correspond to three manually-selected zones of interest.

The region of interest is accordingly selected by setting a minimal subdomain volume V_s and a minimal amount of subvolumes m_e. These values for

the volume limits vary with the shape of the subvolume and are numerically adapted to the curves. We manually choose $V_s = 10^4$, $2\,10^4$ and 10^5 (resp. $m_e = 10$, 120 and 15) for cubic, elongated and plate shape respectively, and

Table (3) shows the RVE size required to achieve a relative precision of 1% for the estimation of various effective physical properties using the three cubic and cuboidal ("plate" and "long") RVE shapes. The relative error for a cubic volume of size 400^3 voxels is given as well. Some of the corresponding variance curves are shown in figures (9), (10), (11), (12), (13) and (14), corresponding resp. to the bulk K and shear G_{zp} elastic moduli for a z-preferred orientation distribution, volume fraction V_V and bulk modulus K for isotropic fibers distribution, and thermal conductivity components k_p and k_z for a planar fibers distribution. As shown in Table 3, the relative error for ten realizations of 400^3 voxels each varies from 0.29% to 1.86%. This confirms a posteriori the validity of the computations undertaken in this work. Furthermore, much improved precision are achieved when using a flat volume shape. For instance, the use of 10 configurations of a flat volume shape (in the xy plane) with a height of 21 voxels is sufficient to estimate numerically the in plane thermal conductivity components of a fiber system with z-preferred direction at 1% relative error. In the literature, nearly parallel fiber systems are often approximated by computations on 2D images of discs, assuming infinite parallel fibers. Considering 2D cuts of the microstructure, the deviation along the z axis is not taken into account. However, the influence of the deviation parameter β in media with a preferred orientation is not negligible. The bottom four lines of table (3) give the ratio of cuboidal RVE sizes with respect to a cubic RVE for a required relative

precision of 1 or 5%. The optimal choice of the RVE depends on the fiber orientation, but also on the considered tensorial component. RVE with flat shapes (of the "plate" type) are best for z-preferred fiber orientation. For an isotropic distribution, the plate (resp. long) shape gives the best result for the elastic moduli (resp. thermal conductivity). For a planar orientation distribution, the plate (resp. long) shape is the best choice for the shear modulus G_{zp} and conductivity component k_z (resp. the thermal conductivity planar component k_p) whereas a cubic shape is preferred for computing the bulk modulus.

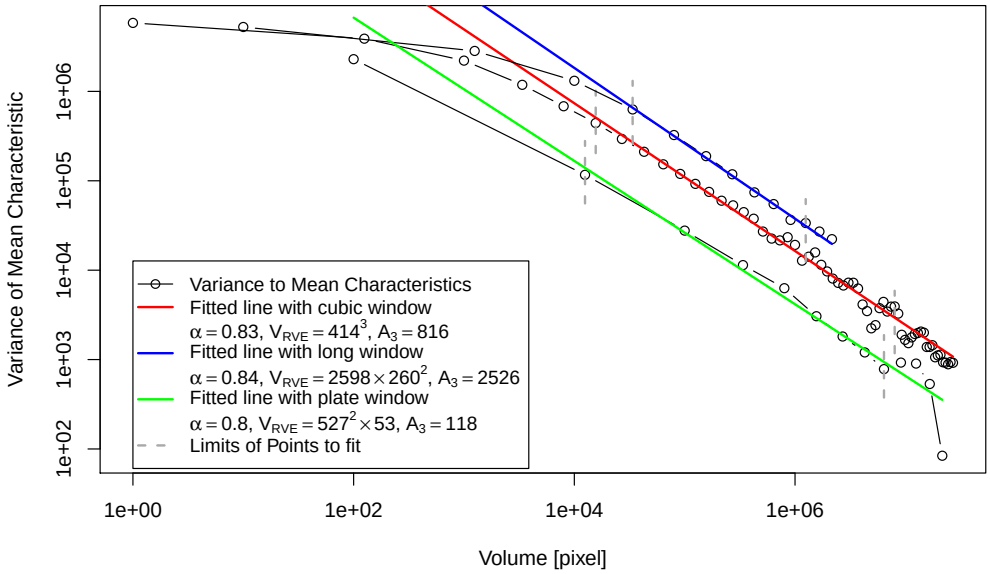

Figure 9: Variance of the apparent bulk modulus K with respect to the volume (in voxels) of cubic, plate and long RVE shapes, for fiber packing with z-preferred orientation distribution ($\beta = 0.05$).

Finally, it is useful to compare the above results with that found in [36], where the authors compute the RVE size of the apparent surface fraction of a

		Z Preferred ($\beta = 0.05$)					Isotropic ($\beta = 1$)				Planar ($\beta = 30$)				
		V_V	K	G_{zp}	k_p	k_z	V_V	K	G	k	V_V	K	G_{zp}	k_p	k_z
CUBIC	$\ell_{\mathrm{RVE}}^{\mathrm{cubic}}(\epsilon_{\mathrm{rel}} = 1\%, n = 1)$	1886	414	832	371	689	1123	477	938	430	1616	509	672	801	438
	$\ell_{\mathrm{RVE}}^{\mathrm{cubic}}(\epsilon_{\mathrm{rel}} = 1\%, n = 10)$	688	164	326	138	258	466	177	375	173	617	189	249	274	153
	$\epsilon_{\mathrm{rel}}(V{=}\,400^3, n = 10)$ [%]	1.86	0.33	0.78	0.29	0.6	1.22	0.39	0.92	0.35	1.68	0.42	0.58	0.67	0.35
	α	0.76	0.83	0.82	0.77	0.78	0.87	0.77	0.84	0.84	0.8	0.77	0.77	0.71	0.73
	A_3	616	816	1086	827	686	1046	559	1031	1031	801	698	687	580	701
LONG	$\ell_{\mathrm{RVE}}^{\mathrm{long}}(\epsilon_{\mathrm{rel}} = 1\%, n = 1)$	771	260	478	158	393	628	207	574	172	1270	312	379	354	301
	$\ell_{\mathrm{RVE}}^{\mathrm{long}}(\epsilon_{\mathrm{rel}} = 1\%, n = 10)$	316	105	175	66	156	239	75	199	65	394	94	122	107	91
	α	0.86	0.84	0.76	0.88	0.83	0.8	0.76	0.73	0.79	0.66	0.64	0.68	0.64	0.64
	A_3	2699	2526	790	2315	2833	468	359	287	337	141	128	185	109	445
PLATE	$\ell_{\mathrm{RVE}}^{\mathrm{plate}}(\epsilon_{\mathrm{rel}} = 1\%, n = 1)$	178	53	109	58	64	239	87	134	116	513	154	84	509	48
	$\ell_{\mathrm{RVE}}^{\mathrm{plate}}(\epsilon_{\mathrm{rel}} = 1\%, n = 10)$	71	20	42	21	26	94	32	55	41	177	50	33	124	18
	α	0.83	0.8	0.8	0.76	0.85	0.82	0.76	0.87	0.74	0.72	0.68	0.83	0.54	0.77
	A_3	205	118	168	241	160	422	286	491	420	503	333	336	191	185
RVE Ratio	$V_{\mathrm{RVE}}^{\mathrm{long}}/V_{\mathrm{RVE}}^{\mathrm{cubic}}(\epsilon_{\mathrm{rel}} = 1\%)$	0.68	2.48	1.90	0.77	1.86	1.75	0.82	2.29	0.64	4.85	2.30	1.79	0.86	3.25
	$V_{\mathrm{RVE}}^{\mathrm{plate}}/V_{\mathrm{RVE}}^{\mathrm{cubic}}(\epsilon_{\mathrm{rel}} = 1\%)$	0.08	0.21	0.22	0.38	0.08	0.96	0.61	0.29	1.96	3.20	2.77	0.20	25.7	0.13
	$V_{\mathrm{RVE}}^{\mathrm{long}}/V_{\mathrm{RVE}}^{\mathrm{cubic}}(\epsilon_{\mathrm{rel}} = 5\%)$	1.12	2.59	1.39	1.30	2.38	1.27	0.77	1.29	0.50	2.07	0.99	1.03	0.53	1.75
	$V_{\mathrm{RVE}}^{\mathrm{plate}}/V_{\mathrm{RVE}}^{\mathrm{cubic}}(\epsilon_{\mathrm{rel}} = 5\%)$	0.12	0.18	0.20	0.36	0.11	0.77	0.57	0.33	1.17	2.05	1.59	0.26	6.16	0.17

Table 3: Size ℓ_{RVE} in number of voxels of representative volume elements for the volume fraction (V_V), bulk (K) and shear (G, G_{pz}) moduli and thermal conductivity (k, k_p, k_z) for transverse isotropic of the z-preferred type (left), planar (right) and isotropic (center) fibers orientation. Three cuboidal RVE shapes are investigated: cubic (top), long (elongated along the z direction, middle) and plate (elongated along the x and y directions, bottom), with, referring to the sizes along the x, y and z directions, $V_{\mathrm{RVE}}^{\mathrm{cubic}} = (\ell_{\mathrm{RVE}})^3$, $V_{\mathrm{RVE}}^{\mathrm{long}} = \ell_{\mathrm{RVE}} \times \ell_{\mathrm{RVE}} \times (10\ell_{\mathrm{RVE}})$, and $V_{\mathrm{RVE}}^{\mathrm{plate}} = (10\ell_{\mathrm{RVE}}) \times (10\ell_{\mathrm{RVE}}) \times \ell_{\mathrm{RVE}}$, resp. The relative errors and number of configurations are noted ϵ_{rel} and n resp.

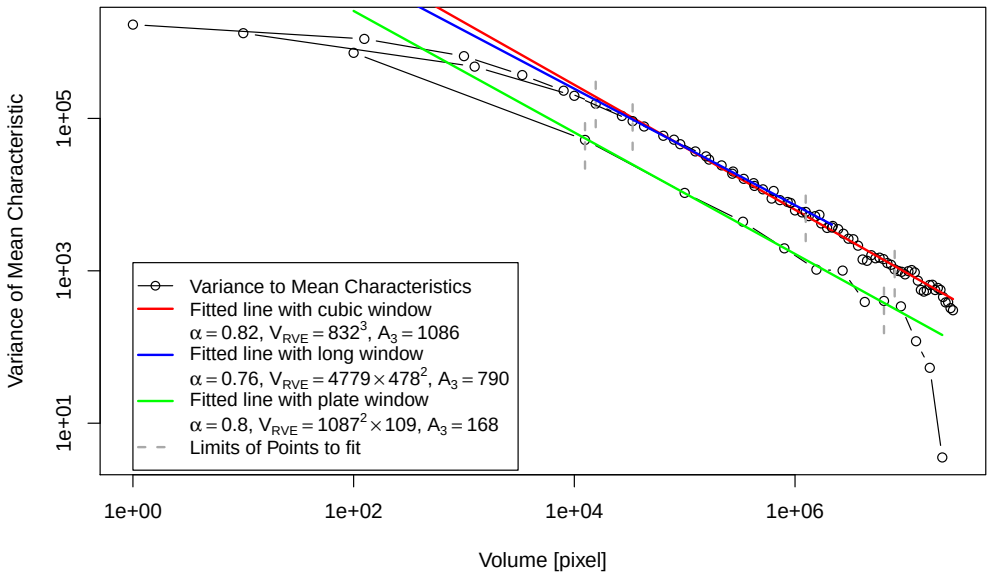

Figure 10: Variance of the apparent shear modulus G_{zp} with respect to the volume (in voxels) of cubic, plate and long RVE shapes, for fiber packing with z-preferred orientation distribution ($\beta = 0.05$).

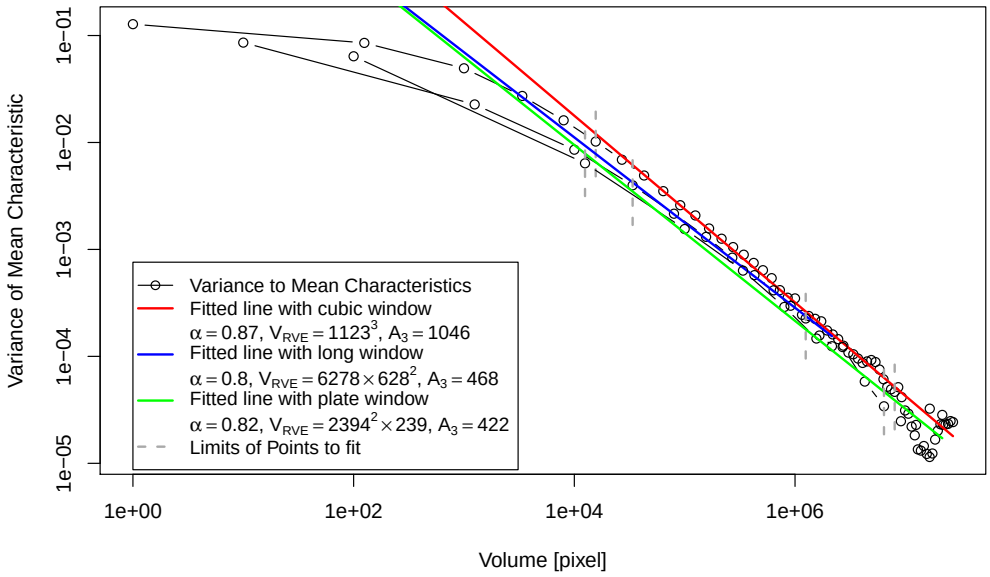

Figure 11: Variance of the apparent volume fraction V_V with respect to the volume (in voxels) of cubic, plate and long RVE shapes, for isotropic fiber distribution ($\beta = 1$).

system of parallel fibers, equivalent to a 2D microstructure, with mean fiber diameter 16 µm. The authors determined the RVE as a surface of 1311 µm sidelength, for $n = 100$ realizations and a relative error of 1%. This is to be compared with a fibrous microstructure with plate shape, as considered in this work, where the fiber radius is 5.44 pixels. Assuming a voxel sampling of 1.47 µm voxel, and flattening the volume to 1 voxel thickness, a 2D section is recovered. Such conversion results in a 2D section of 1687 µm sidelength. As the fibers in the 3D stochastic model are not completely parallel nor straight, it is reasonable that the RVE is slightly higher than in [36].

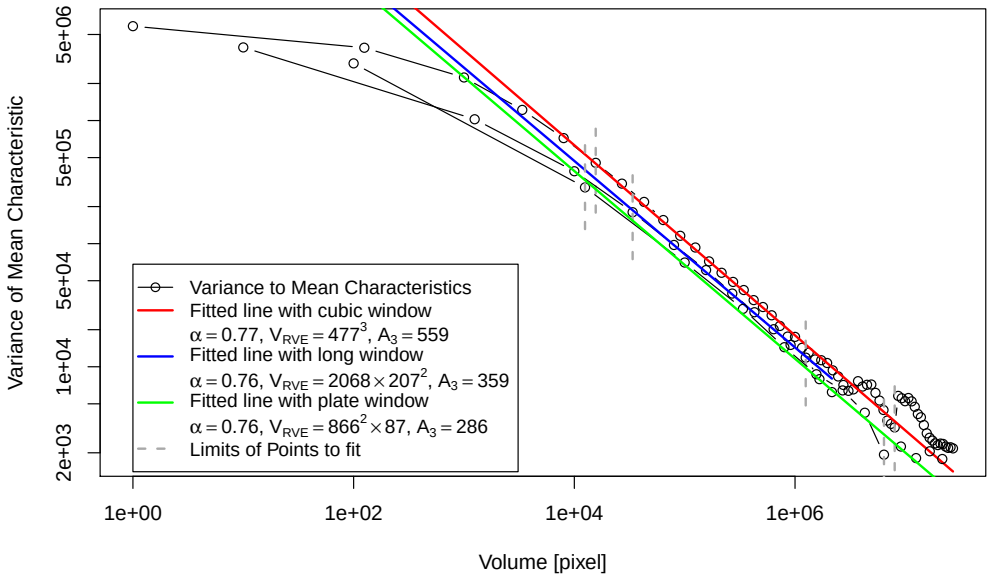

Figure 12: Variance of the apparent bulk modulus K with respect to the volume (in voxels) of cubic, plate and long RVE shapes, for isotropic fiber distribution ($\beta = 1$).

5. Effective response vs. fiber distributions

FFT results for the elastic and thermal responses of various fibrous microstructures are represented in figures (15) to (19) as well as analytical bounds and estimates. The elastic and thermal properties are bounded by the general Reuss and Voigt or by the Wiener bounds only (magenta lines). The response of the isotropic microstructure is also bounded by the sharpest 3D Hashin and Shtrikman bounds (black dots), whereas the 2D HS bounds (orange lines) and the self-consistent estimates (cyan dots) are shown for comparison.

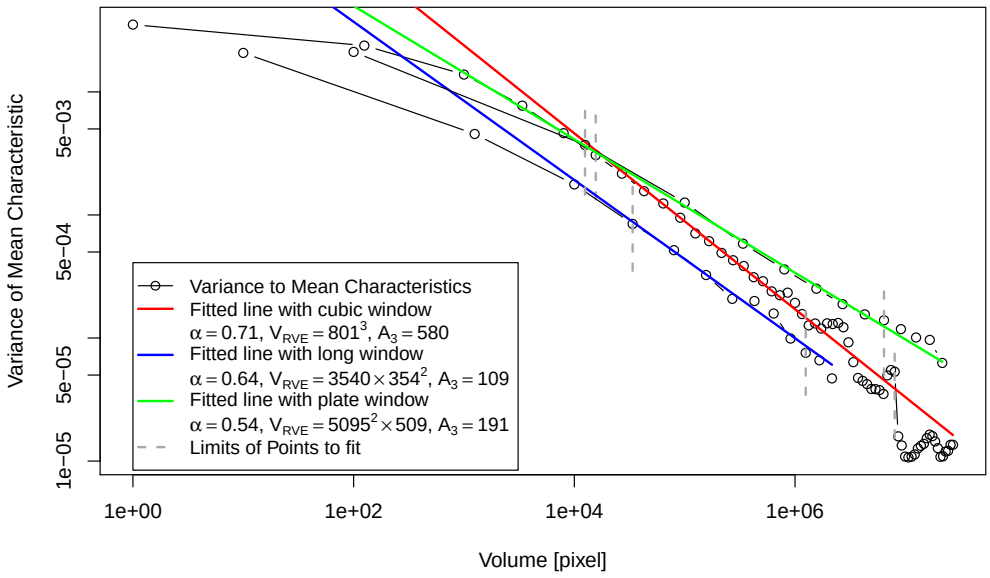

Figure 13: Variance of the apparent planar thermal conductivity component k_p with respect to the volume (in voxels) of cubic, plate and long RVE shapes,for a planar orientation distribution ($\beta = 30$) of fibers.

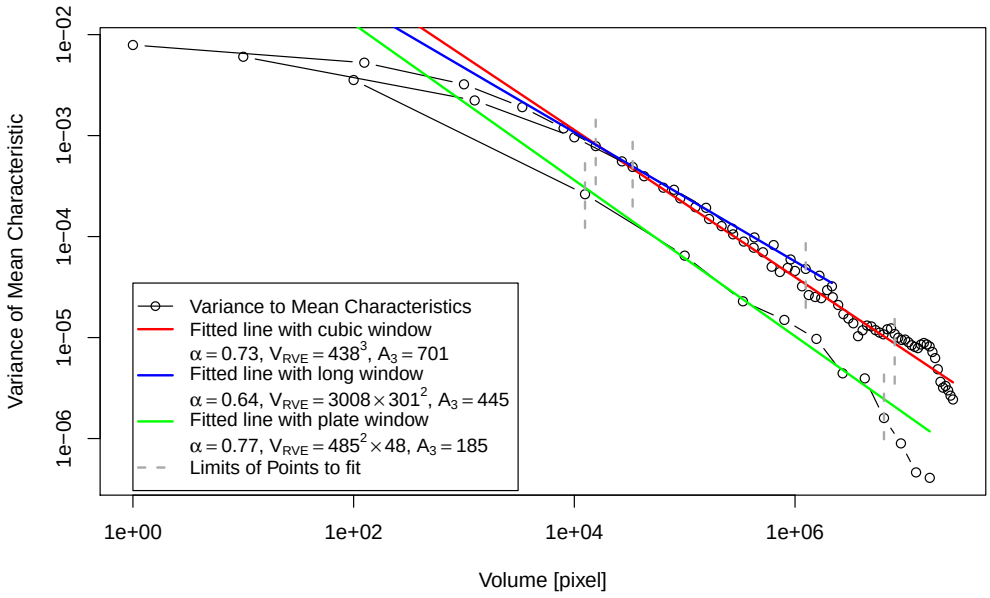

Figure 14: Variance of the apparent transverse thermal conductivity component k_z with respect to the volume (in voxels) of cubic, plate and long RVE shapes,for a planar orientation distribution ($\beta = 30$) of fibers.

5.1. Young's moduli

Results for Young's moduli are shown in figure 15. As expected, the material is reinforced in the direction of the fibers. Since the fibers are stiffer than the matrix, the stiffness of the composite is higher in the preferred direction of the fibers. For a planar orientation distribution the Young's modulus is also stronger in the planar directions, but the difference is smaller compared to z-preferred orientation distribution. The right part of the parameter sets, with varying $\kappa_{1,2}$ values describes different fiber curvatures. These parameter sets are divided in four sets, which are ordered by increasing global straightness or decreasing global bending. The microstructures in each set are ordered by increasing local straightness. The stiffness in the z-direction increases with the fiber straightness. In the y direction only a small decrease is observed, whereas no visible trend apepars in the x direction.

As expected, the Boolean model of cylinders, with straight fibers and more connected fiber system, always has higher stiffness than the corresponding model with bending fibers. We note however that Boolean media are not realistic models of glass fibers, where no interpenetration occures. Overall, the properties of the real microstructure and of the corresponding orthotropic model are close to each other, which confirms that the structure of the real material is correctly simulated by the stochastic model.

5.2. Poisson's ratios

The Poisson ratios $\nu_{xy,yz,xz}$ are represented in figure (16). They strongly depend on the fibers directions. For tranversely isotropic fibers distribution with $\beta < 1$, they vary between 0.12 and 0.51. Note that, for anisotropic media the Poisson ratios $\nu_{xy,yz,xz}$ are not constrained between 0 and 0.5 as

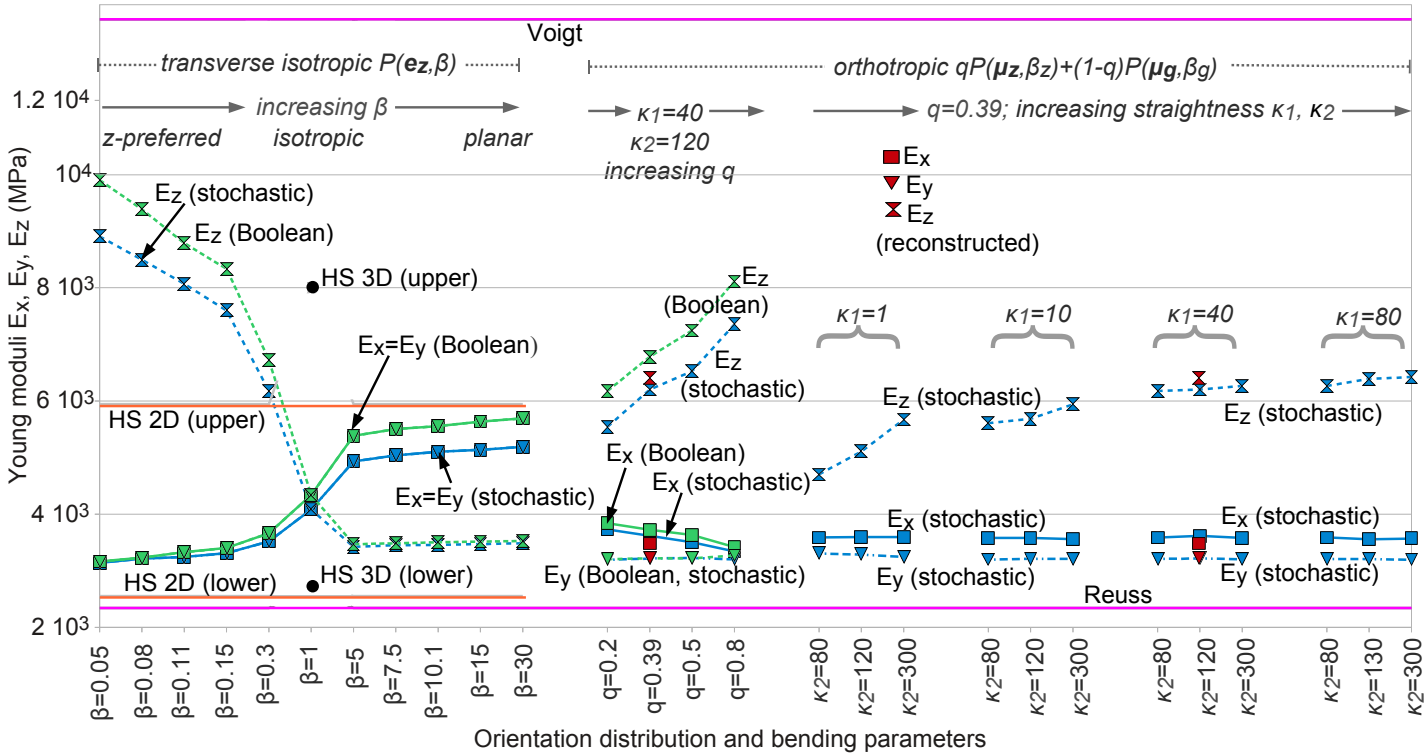

Figure 15: Young moduli E_x (□), E_y (▽) and E_z (⧖) of various transversely-isotropic (left) and orthotropic (right) fibers distributions: FFT results for the stochastic (blue) and Boolean (green) models, and for the reconstructed material (red); Voigt and Reuss bounds (magenta), 2D (orange) and 3D (black dots) Hashin and Shtrikman (HS) bounds. Fibers are much stiffer than the matrix, with elastic properties given in table (2). In all microstructures, the volume fraction is $V_V = 15\%$, the radiuses follow the distribution $\mathcal{N}(19\,\mu\text{m}, 2.1\,\mu\text{m})$ and the mean fiber length is $\widehat{L} = 1.19\,\text{mm}$. The straightness parameters are $\kappa_1 = 40$ and $\kappa_2 = 120$ except when noted.

for an isotropic medium. Less variation is observed for a planar orientation distribution or for higher fiber curvature.

5.3. Shear moduli

FFT results for the elastic shear modulus as shown in Figure 17 exhibit high values in the planar directions of the girdle orientation. This effect is expected as the stiff fibers in the planar direction is opposed to the applied strain, when shear strain loading is applied. The mixed β-distributions have an intermediate behavior. The values for G_{zx} are slightly higher, because the zx plane is closest to the plane in which the girdle orientation distribution is concentrated. Consistently with results observed in [36], the shear modulus is close to the lower Hashin-Shtrikman bound for z preferred materials. Increasing the fiber bending results in a slight decrease of the shear modulus.

5.4. Bulk modulus

The bulk modulus in Figure 18 is the response to hydrostatic uniform pressure on the material. Accordingly, it is not very sensitive to the different orientation distributions. The response value is mainly dependent on the volume fraction, which is constant in all models. It should be noted however that bending tends to decrease the bulk modulus. The responses for the boolean model are slightly higher, since the fiber system is connected and therefore more resistant to the applied strain. Due to some defects in the binarization of the original dataset, some false connections occur and therefore the simulation on the binarized image tends to a slightly too high

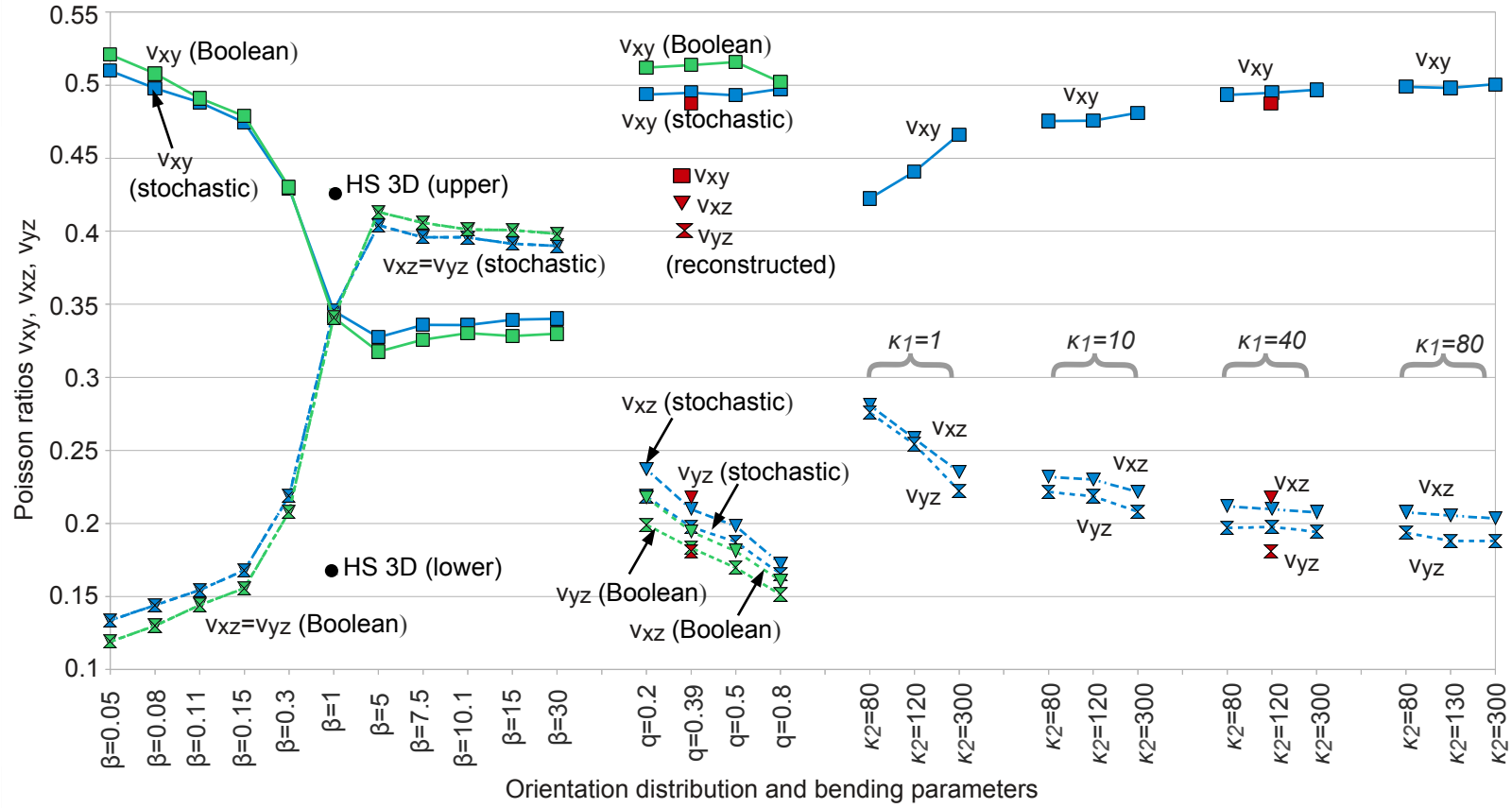

Figure 16: Continuation of figure (15): Poisson ratios ν_{xy}, ν_{xz} and ν_{yz}

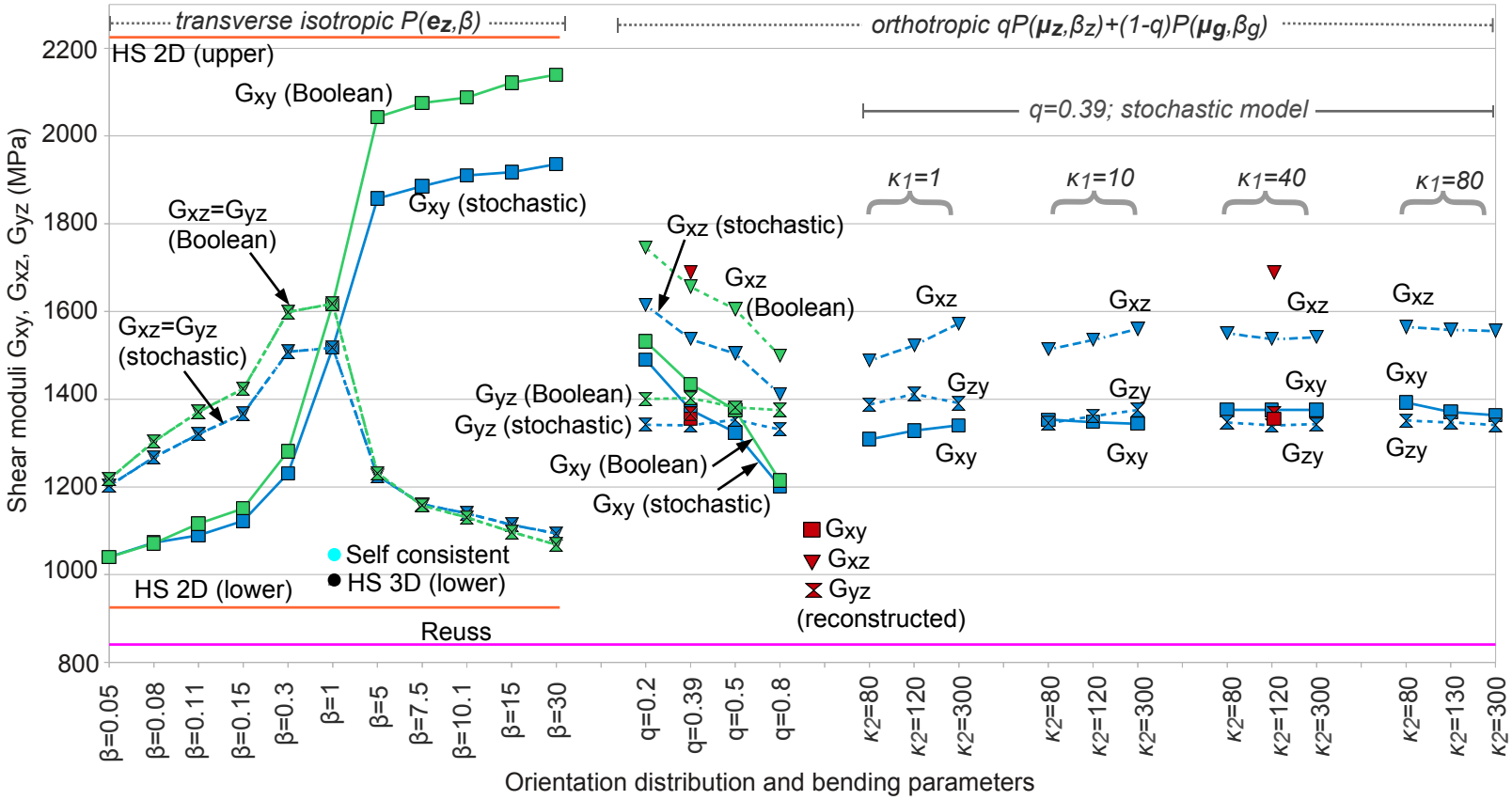

Figure 17: Continuation of figure (15): shear moduli G_{xy}, G_{xz} and G_{yz}. Self-consistent estimate represented by a cyan-colored dot.

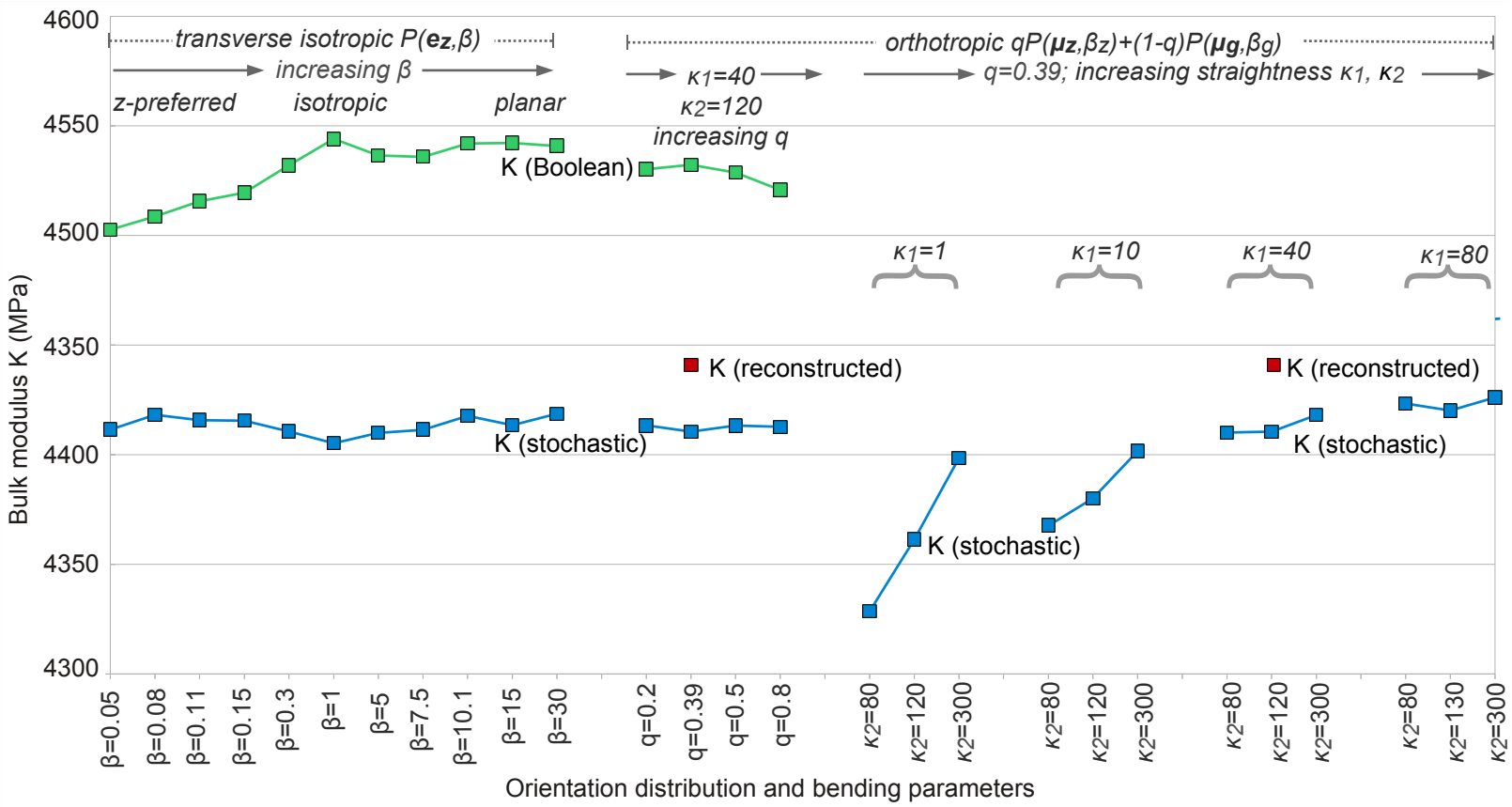

Figure 18: Continuation of figure (17): bulk modulus κ.

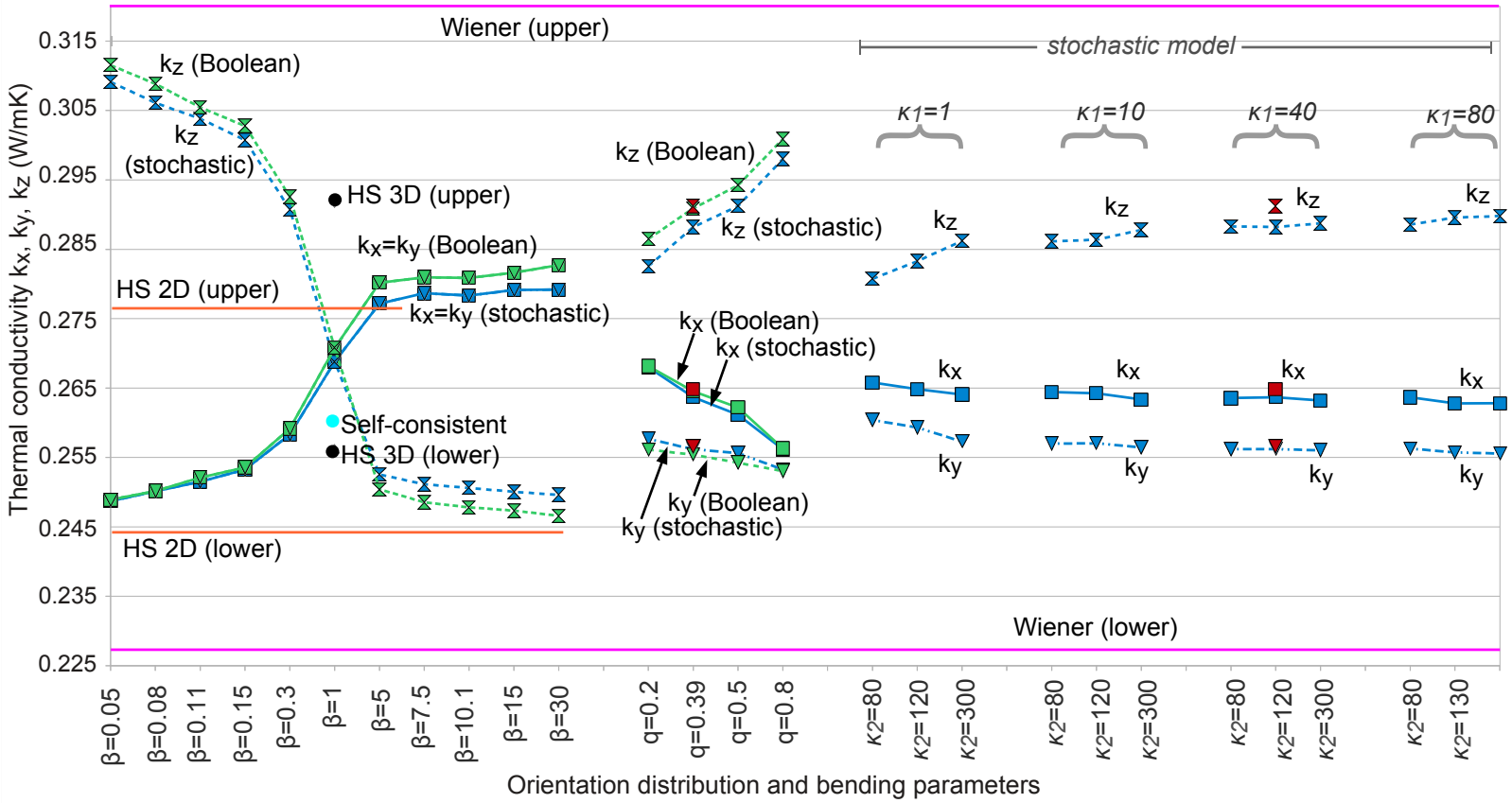

Figure 19: Continuation of figure (17): thermal conductivity components k_x, k_y and k_z. Wiener bounds in magenta.

result. The bulk modulus is relatively close to the lower bounds for all types of materials.

5.5. Thermal conductivity

FFT results for the thermal conductivity are given in Figure 19. The effective conductivity is high along the fiber directions as the very long fibers conduct heat through the material. As observed in [36], the thermal conductivity is close to the lower Hashin-Shtrikman bound in the directions orthogonal to the fiber arrangement, where the thermal isolation provided by the matrix material is favored. In that respect, fibers are usually in a planar configuration in materials used in the enclosure of boats or airplanes, to provide thermal isolation between the interior and exterior. It is emphasized that the estimated physical properties of the real microstructure and of our "mixed" stochastic model are nearly equal for all physical and thermal responses, which confirms that the structure of the real material is consistent with the adapted stochastic model.

6. Conclusion

In this work, set in the framework of virtual material design, the mechanical and thermal simulation of a fibrous material has been undertaken. For the application on glass fiber reinforced polymers, experimental data was used to construct realistic material models up to the predictions of their physical properties. Such analysis necessitates the estimation of the relevant microstructure parameters, from local radius and orientation analysis, over fiber separation techniques, up to stochastic modeling. The influence of the

geometrical parameters on the macroscopic properties has been examined and interpreted in terms of expected behavior.

Geometrical characteristics such as the fiber curvature and the mixed β -distribution are adequately estimated using the reconstructed fiber system. Making use of the stochastic model, it is possible to create virtual materials by generating realizations with varying geometrical parameters, whose physical properties are readily computed using FFT methods. The computation of the representative volume element confirms that the number of realizations equal to 10, and overall volume discretization of 400^3 voxels have sufficient accuracy. Still, the computation of the RVE is to be improved using larger observation subdomains.

The following phenomenological interpretations are made: the fiber arrangement strongly influences the elastic and thermal responses. In contrast, these physical responses are generally less sensitive to the fiber curvature. Furthermore, comparison with a model of Boolean cylinders allows to estimate the influence of overlap. Finally, it has been found that in general, the effective properties of the rebuilt fiber packing match those of the real material provided the necessary geometrical parameters are set accordingly. Such study allows in particular to optimize the effective properties with respect to the application; this is especially useful for anisotropic materials, where minimal mechanical responses are required in the weakest modes.

In that respect, the introduction of additional microstructure parameters such as the aspect ratio, local alignment, or multiple layers of varying orientation distributions could lead to a wider range of useful mechanical and thermal properties.

7. Acknowledgements

This work was developed in the scope of the cooperation of Mines ParisTech, Technical University of Kaiserslautern and Fraunhofer Institute for Industrial Mathematics in Kaiserslautern. Financial support was provided by the Fraunhofer ITWM in Kaiserslautern and the Institute Carnot M.I.N.E.S. The work of this manuscript includes images of glass fiber reinforced polymers from samples provided by the IVW in Kaiserslautern recorded at the BAMline (BESSY II, Berlin, Germany). Softwares and libraries as Morph-M and Morph-Hom (developed at CMM - Center of Mathematical Morphology in Fontainebleau) serve as toolboxes for the creation of algorithms presented in this paper. Visualizations use the open source VTK library.

[1] R. M. Mayer, Design with reinforced plastics, Springer, 1993.

[2] East Coast Fibreglass Supplies, Guide to glass reinforced plastics, `www.ecfibreglasssupplies.co.uk/t-GlassReinforcedPlastics.aspx` (accessed sep. 30, 2013). (2010).

[3] H. Altendorf, D. Jeulin, 3D directional mathematical morphology for analysis of fiber orientations, Image Analysis and Stereology 28 (2009) 143–153.

[4] H. Altendorf, D. Jeulin, Fiber separation from local orientation and probability maps, in: M. Wilkinson, J. Roerdink (Eds.), Abstract book of the 9th Int. Symp on Math. Morph. (ISMM'2009), University of Groningen, The Netherlands, 2009, pp. 33–36, `www.cs.rug.nl/ ISMM09/ISMMabstractbook.pdf` (accessed Sep. 30, 2013).

[5] H. Altendorf, E. Decencière, D. Jeulin, P. D. S. Peixoto, A. Deniset-Besseau, E. Angelini, G. Mosser, M.-C. Schanne-Klein, Imaging and 3D morphological analysis of collagen fibrils, Journal of Microscopy 247 (2012) 161–175.

[6] H. Altendorf, 3D morphological analysis and stochastic modeling of random fiber networks – applied on glass fiber reinforced composites, Ph.D. thesis, Mines ParisTech, TU Kaiserslautern and Fraunhofer ITWM, available at HAL : pastel-00667398 (nov. 2011).

[7] K. Schladitz, S. Peters, D. Reinel-Bitzer, A. Wiegmann, J. Ohser, Design of acoustic trim based on geometric modeling and flow simulation for non-woven, Computational Materials Science 38 (1) (2006) 56–66.

[8] J. Ohser, K. Schladitz, 3D Images of Materials Structures – Processing and Analysis, Wiley VCH, Weinheim, 2009.

[9] H. Altendorf, D. Jeulin, Stochastic modeling of a glass fiber reinforced polymer, Lecture Notes in Computer Science 6671 (2011) 439–450.

[10] S. Kärkkäinen, J. Nyblom, A. Miettinen, T. Turpeinen, P. Pötschke, A stochastic shape model for fibres with an application to carbon nanotubes, in: Proc. of 10th European Congress of Stereology and Image Analysis, 2008.

[11] S. Kärkkäinen, A. Miettinen, T. Turpeinen, J. Nyblom, P. Pötschke, J. Timonen, A stochastic shape and orientation model for fibres with an application to carbon nanotubes, Image Analysis and Stereology 31 (1) (2012) 17–26.

[12] D. Ko, Robust estimation of the concentration parameter of the von Mises-Fisher distribution, in: Annals of Statistics, Vol. 20, 1992, pp. 917–928.

[13] A. Banerjee, I. S. Dhillon, J. Ghosh, S. Sra, Clustering on the unit hypersphere using von Mises-Fisher distributions, J. Mach. Learn. Res. 6 (2005) 1345–1382.

[14] H. Altendorf, D. Jeulin, Random-walk-based stochastic modeling of three-dimensional fiber systems, Phys. Rev. E 83 (4) (2011) 041804.

[15] H. Altendorf, D. Jeulin, 3D modeling of dense packings of bended fibers, in: Proc. of ICS 2011.

[16] D. Gross, T. Seelig, Bruchmechanik - Mit Einführung in die Mikromechanik, Springer, 2011.

[17] T. Mura, Micromechanics of defects in solids, Martinus Nijhoff Publishers, 1987.

[18] S. Nemat-Nasser, M. Hori, Micromechanics: Overall Properties of Heterogeneous Materials, North-Holland Series in Applied Mathematics and Mechanics, 1998.

[19] J. Aboudi, Mechanics of Composite materials - A unified Micromechanical Approach, Elsevier Science, 1991.

[20] T. Zohdi, P. Wriggers, An introduction to computational micromechanics, Springer, 2008.

[21] S. Schmauder, L. Mishnaevsky, Micromechanics and Nanosimulation of Metals and Composites, Springer, 2008.

[22] E. Barbero, Finite Element Analysis of Composite Materials, CRC Press, 2007.

[23] J. Mandel, Cours de Mcanique des Milieux Continus, Gauthiers Villars eds., 1966.

[24] J.-C. Michel, H. Moulinec, P. Suquet, A computational scheme for linear and non-linear composites with arbitrary phase contrast, Int. J. Numer. Meth. Engng. 52 (1-2) (2001) 139–160.

[25] H. Moulinec, P. Suquet, Comparison of FFT-based methods for computing the response of composites with highly contrasted mechanical properties, Phys. Rev. B 338 (1–4) (2003) 58–60.

[26] F. Willot, Y. Pellegrini, M. Idiart, P. Castañeda, Effective-medium theory for infinite-contrast two-dimensionally periodic linear composites with strongly anisotropic matrix behavior: Dilute limit and crossover behavior, Physical review B 78 (10) (2008) 104111.

[27] F. Willot, Y.-P. Pellegrini, Fast fourier transform computations and build-up of plastic deformation in 2D, elastic-perfectly plastic, pixelwise disordered porous media, in: Continuum Models and Discrete Systems: CMDS 11: Proceedings of the International Symposium Held in Paris July 30th-August 3rd 2007, Dominique Jeulin and Samuel Forest eds., École des Mines, Paris, 2008.

[28] D. J. Eyre, G. W. Milton, A fast numerical scheme for computing the response of composites using grid refinement, The European Physical Journal Applied Physics 6 (1) (1999) 41–47.

[29] F. Willot, D. Jeulin, Elastic behavior of composites containing Boolean random sets of inhomogeneities, International Journal of Engineering Science 47 (2) (2009) 313–324.

[30] C. Dunant, B. Bary, A. Giorla, C. Péniguel, J. Sanahuja, C. Toulemonde, A. Tran, F. Willot, J. Yvonnet, A critical comparison of several numerical methods for computing effective properties of highly heterogeneous materials, Advances in Engineering Software 58 (2013) 1–12.

[31] Z. Hashin, S. Shtrikman, A variational approach to the theory of the elastic behaviour of multiphase materials, Journal of the Mechanics and Physics of Solids 11 (2) (1963) 127–140.

[32] G. W. Milton, The Theory of Composites, Cambridge Univ. Press, Cambridge, 2002.

[33] R. Hill, A self-consistent mechanics of composite materials, Journal of the Mechanics and Physics of Solids 13 (4) (1965) 213–222.

[34] T. Kanit, S. Forest, I. Galliet, V. Mounoury, D. Jeulin, Determination of the size of the representative volume element for random composites : statistical and numerical approach, International Journal of Solids and Structures 40 (2003) 3647–3679.

[35] T. Kanit, F. N'Guyen, S. Forest, D. Jeulin, M. Reed, S. Singleton, Apparent and effective physical properties of heterogeneous materials: Rep-

resentativity of samples of two materials from food industry, Comput. Methods Appl. Mech. Engrg. 195 (2006) 3960–3982.

[36] M. Oumarou, D. Jeulin, J. Renard, Etude numérique et statistique du comportement d'un composite thermoplastique, Revue des composites et des matériaux avancés 21 (2) (2011) 221–254.

[37] D. Jeulin, Variance scaling of Boolean random varieties, `hal.archives-ouvertes.fr/hal-00618967` (accessed Sep. 30, 2013).

[38] F. Willot, L. Gillibert, D. Jeulin, Microstructure-induced hotspots in the thermal and elastic responses of granular media, International Journal of Solids and Structures 50 (10) (2013) 1699–1709.